

Squall Line Response to Coastal Mid-Atlantic Thermodynamic Heterogeneities

KELLY LOMBARDO^a

^a *Department of Meteorology and Atmospheric Science, The Pennsylvania State University, University Park, Pennsylvania*

(Manuscript received 14 February 2020, in final form 22 September 2020)

ABSTRACT: Idealized 3D numerical simulations are used to quantify the impact of moving marine atmospheric boundary layers (MABLs) on squall lines in an environment representative of the U.S. mid-Atlantic coastal plain. Characteristics of the MABL, including depth and potential temperature, are varied. Squall lines are most intense while moving over the deepest MABLs, while the storm encountering no MABL is the weakest. Storm intensity is only sensitive to MABL temperature when the MABL is sufficiently deep. Collisions between the storm cold pools and MABLs transition storm lift from surface-based cold pools to wavelike features, with the resulting ascent mechanism dependent on MABL density, not depth. Bores form when the MABL is denser than the cold pool and hybrid cold pool–bores form when the densities are similar. While these features support storms over the MABL, the type of lifting mechanism does not control storm intensity alone. Storm intensity depends on the amplification and maintenance of these features, which is determined by the ambient conditions. Isolated convective cells form ahead of squall lines prior to the cold pool–MABL collision, resulting in a rain peak and the eventual discrete propagation of the storms. Cells form as storm-generated high-frequency gravity waves interact with gravity waves generated by the moving marine layers, in the presence of reduced stability by the squall line itself. No cells form in the presence of the storm or the MABL alone.

KEYWORDS: Convective storms; Convective-scale processes; Cloud resolving models

1. Motivation

Squall lines and their associated hazards (flash flooding, high winds, frequent lightning, small hail, tornadoes) impact a large number of coastal regions globally: the eastern United States (Lombardo and Colle 2010, 2011, 2012, 2013); the eastern Mediterranean including Israel (Lensky and Schiff 2007) and Turkey (Kömüçü et al. 1998); the western Mediterranean, including Spain (Tuduri and Ramis 1997; van Delden 1998; Cohuet et al. 2011), France (Morel and Senesi 2002a,b), and Italy (Kurz and Fontana 2004); China (Meng et al. 2013) and islands within the South China Sea (Wang and Carey 2005); the Philippines and Maritime Continent (Li et al. 2012; Ichikawa and Yasunari 2007; Yuan and Houze 2010); regions of South America, such as Brazil (Garstang et al. 1994; Greco et al. 1994; Mattos and Machado 2011), Argentina and Uruguay (Salio et al. 2007), Columbia and Ecuador (Warner et al. 2003); southern (Blamey and Reason 2009) and western Africa (Futyan and Genio 2007; DeLonge et al. 2010); and Australia (Drosowsky et al. 1989). As these deep convective storms move over coastal regions, they are impacted by the underlying surface and associated lower-tropospheric horizontal heterogeneities, which can include gradients in boundary layer temperature and moisture, low-level wind, and surface friction (Taylor et al. 1997; Clark et al. 2003, 2004; Lericos et al. 2007; DeLonge et al. 2010; Wolters et al. 2010; Lombardo and Colle 2013; Peters and Hohenegger 2017; Lombardo and Kading 2018, hereafter LK18). The dynamic interconnectivity between squall lines and the coastal environment results in particularly challenging forecasts, and motivates the need to quantify storm responses to these heterogeneities.

While advancements have been made, the scope of the scientific challenge is large. For example, a range of ambient thermodynamic and vertical wind shear profiles can support squall line organization (Weisman and Klemp 1982, hereafter WK82; Weisman and Klemp 1984; Rotunno et al. 1988; LeMone et al. 1998). Each environment within this range defines the inherent characteristics of a storm, such as internal thermodynamic processes, dynamic circulations, storm intensity, lifetime, and hazards. Each unique storm will respond differently to each type of coastal horizontal heterogeneity, which have their own range of magnitudes and structures. This sizable parameter space necessitates the use of systematic studies to isolate the impact of each feature within different base-state environments. This work quantifies squall line response as it encounters a moving marine atmospheric boundary layer (MABL), highlighting dynamic physical processes supporting a discrete propagation prior to the encounter and storm movement once over the stable layers, as well as the sensitivity of storm intensity to differences in MABL temperature and depth, determining characteristics that are the most influential on squall line predictability.

a. Environment horizontal heterogeneities

Variations in the coastal surface (i.e., land versus ocean) modify the overlying tropospheric thermodynamic instability and vertical wind shear. Observational and numerical studies have arrived at differing conclusions regarding the relative role of these tropospheric variations on coastal squall lines. The dominant role of instability gradients has been argued in the context of an observed land-based early morning mesoscale convective system (MCS) that crossed the West African coastline (DeLonge et al. 2010). Surface fluxes modified the spatial distribution of instability, specifically the development of a high-CAPE, low-CIN environment over land, to which the

Corresponding author: Kelly Lombardo, lombardo@psu.edu

DOI: 10.1175/JAS-D-20-0044.1

© 2020 American Meteorological Society. For information regarding reuse of this content and general copyright information, consult the AMS Copyright Policy (www.ametsoc.org/PUBSReuseLicenses).

Authenticated kelly.lombardo@psu.edu | Downloaded 04/12/21 02:38 PM UTC

authors attribute the storm's robustness upon its coastal arrival. Weaker ocean sensible heat fluxes contributed to smaller CAPE and larger CIN offshore, ultimately causing storm decay. Given that the horizontal gradient in vertical wind shear was minimal and supportive of MCSs both inland and offshore, it was deemed less important.

Other studies have shown that coastal horizontal heterogeneities in vertical wind shear dominate storm response (Lericos et al. 2007; Lombardo and Colle 2013). Numerically simulated squall lines in an idealized environment representative of western Florida (United States) were shown to decay moving onshore due a reduction in the lower-tropospheric vertical wind shear (Lericos et al. 2007). During both the simulated "nighttime" (i.e., $T_{\text{landscf}} < T_{\text{oceansfc}}$) and "daytime" (i.e., $T_{\text{landscf}} > T_{\text{oceansfc}}$), the near-surface vertical wind shear over land was smaller than over water due to either the development of a daytime sea breeze circulation, limited momentum exchange across the top of the "nocturnal" inversion combined with larger land friction, and/or modification of the environment by the storm itself. Variations in instability were deemed inconsequential given the large, most-unstable CAPE (MUCAPE) over land during both daytime and nighttime, and the availability of high- θ_e air above the 300-m-deep nocturnal stable layer. Favorable instability in the presence of reduced wind shear resulted in upshear tilted storm updrafts, which promoted storm decay (Rotunno et al. 1988; Weisman et al. 1988; Weisman and Rotunno 2004).

Similarly, the importance of vertical wind shear was illustrated in the analysis of two New England (United States) squall lines that originated over land and moved over the coastal Atlantic (Lombardo and Colle 2013). It is often assumed that most storms decay upon coastal crossing due to the MABL-reduced instability, though this was not the case in the aforementioned squall lines. One storm decayed at the coast as it encountered a substantial reduction in wind shear over the ocean, despite the moderate surface-based and elevated instability (i.e., MUCAPE = 1200–1600 J kg⁻¹) offshore. The other storm survived as it moved into an environment with lower stability (i.e., MUCAPE = 400–800 J kg⁻¹), but larger low-level vertical wind shear. To assess the role of the offshore wind shear, the Atlantic Ocean was removed in the simulated decaying-storm event. In the absence of an ocean, CAPE over the former ocean surface increased, though vertical wind shear through the depth of the storm cold pool decreased by 30%. Despite the larger instability, the squall line decayed. The relationship between wind shear and the storm's cold pool characteristics were implicitly linked to the coastal crossing outcomes following arguments posed in Rotunno et al. (1988). In an additional experiment, the simulated decaying storm became more intense and longer-lived as it moved offshore when its cold pool depth and negative temperature perturbation was reduced, attributed to a "better balance" of the cold pool and ambient wind shear circulations (Lombardo and Colle 2013).

b. Marine atmospheric boundary layer

Offshore squall line survival has also been considered in the context of the source of parcel lift, in the presence of favorable shear and some amount of instability (Lericos et al. 2007;

Lombardo and Colle 2013; LK18). Daytime squall lines over land are typically supported by surface-based cold pool forced ascent, though this may change once the storm encounters a moving MABL (i.e., sea breeze). Lift can transition from a cold pool to a bore after the cold pool collides with the sea breeze (Wakimoto and Kingsmill 1995; Kingsmill and Crook 2003; Lombardo and Colle 2013; LK18). A bore is a wavelike disturbance that can form as two stably stratified fluids, of equal or differing densities, encounter one another (Simpson 1982; Rottman and Simpson 1989). In the atmosphere, bores have been shown to form through the collision between two density currents, such as sea breezes and thunderstorm outflows (Clark 1983, 1984; Smith 1986; Noonan and Smith 1986, 1987; Kingsmill and Crook 2003), as well as in association with nighttime mesoscale convective systems in the central Plains as a storm cold pool interacts with the nocturnal inversion (Haase and Smith 1984; Doviak and Ge 1984; Carbone et al. 1990; Fulton et al. 1990; Koch et al. 1991; Knupp 2006; Haghi et al. 2019). For density currents that collide with one another, bores generated may move in opposite directions away from the source region (Clark 1983; Smith 1986); One propagates along the interface between the denser gravity current and free troposphere ahead of the now elevated, trailing lighter fluid, and the other travels along the interface between the less dense fluid, which is undercut by the denser fluid, and overlying troposphere (Clark 1984; Kingsmill and Crook 2003). Unlike the original density currents, classical bores transport no mass, though, hybrid structures, which transport density current air that has mixed into the leading edge of the bore have been observed (Fulton et al. 1990; Haase and Smith 1989). Bores have been shown to play an important role in the generation and maintenance of convection, lifting air parcels as high as 900 m (Parsons et al. 2019; Loveless et al. 2019). Therefore, for bores that form in the coastal environment, the associated lift can support deep convective storms as they move along the stable MABL away from the coast.

Though it has been difficult to develop predictability metrics for coastal bore development based on observed case studies (Wakimoto and Kingsmill 1995; Kingsmill and Crook 2003), more recent numerical modeling work (LK18) proposed that buoyancy differences between the storm cold pool and MABL offer insight. For a MABL with lower (i.e., more negative) buoyancy than the storm cold pool, the collision produced a bore. In the reverse scenario, forcing remained a cold pool. When the buoyancy of the two was similar, forcing transitioned to a hybrid cold pool–bore. These conclusions were drawn from 2D simulations initialized in a single environment (WK82), which begs the question of the robustness of these results in 3D simulations with other base states.

c. Nocturnal boundary layer

Given similarities between MABLs and stable nocturnal boundary layers, a brief comparison is warranted. A number of studies have quantified the impact of nocturnal boundary layers on inland MCSs, including the importance of storm-generated bores in supporting preexisting or initiating new convection (e.g., Dudhia et al. 1987; Crook and Moncrieff 1988; Schmidt and Cotton 1990; Buzzi et al. 1991; Knupp 2006;

Parker 2008; Schumacher 2009; French and Parker 2010; Marsham et al. 2011; Trier et al. 2011; Schumacher 2015; Parsons et al. 2019). Bores can form as convective downdrafts impinging on the top of a mature nocturnal boundary layer (e.g., Marsham et al. 2011), or during the development of the stable layer, supporting storms once the temperature of the layer approaches that of the storm cold pool (Parker 2008). More recently, results from the Plains Elevated Convection at Night (PECAN) field campaign (Geerts et al. 2017) show that *elevated* bores can develop within an inversion layer aloft in association with cold pool layer lifting (Zhang et al. 2020). New convection formed behind the bore due to enhanced instability in the bore-modified environment leading to the discrete propagation of the MCS. Bores within the surface-based nocturnal layer can induce CI as well, by reducing environmental CIN and the level of free convection (LFC; Loveless et al. 2019; Parsons et al. 2019).

Although parallels can be drawn between marine and nocturnal boundary layers, there can be notable differences regarding the interaction between a storm and each type of stable layer. Coastal squall line outflow abruptly encounters a sea breeze in the presence or absence of radiation, and vigorously perturbs the stable layer from the side. Nocturnal squall lines can vertically perturb a gradually developing or mature stable nocturnal layer from above. Comparing these two scenarios, the mechanisms by which bores form differ, which potentially has implications for the resulting storm response. Often, however, strong nocturnal boundary layer horizontal temperature gradients exist inland, an environment much like the coastal zone.

d. Isolated cell development downstream of coastal squall lines

An interesting precipitation evolution has been observed to occur as squall lines approach the mid-Atlantic and New England coastlines. Radar reflectivity has documented the development of isolated convective cells forming 5–50 km downstream of the primary squall lines, prior to their coastal crossing attempt. For example, in their study of two observed northeastern U.S. coastal squall lines, Lombardo and Colle (2013) presented evidence of the development of just a few isolated cells to a field of cells straddling the coastline parallel to the main storms (their Figs. 6 and 14). The displaced generation of this new convection may increase coastal precipitation, beyond that associated with the main squall line, and cause precipitation to fall sooner than anticipated based on the storm translational speed. Since this was not the focus of the study, the associated physical processes went unexplored.

e. Approach

Our holistic goal is to identify robust similarities and differences in storm-scale physical processes associated with coastal storms across a broad range of MABL characteristics and environmental conditions. This work addresses changes to coastal squall line dynamics in 3D and in an environment representative of the coastal midlatitudes, specifically the mid-Atlantic, given the large population and frequency of coastal squall lines in this region. Ultimately, quantifying consistent responses across a broad range of conditions may lead to

improvements in predictability, including the associated hazards. Section 2 describes the idealized numerical configuration, including the MABL parameter space. Section 3 presents evidence of the different ascent mechanisms that support storms over the various MABLs, the associated ambient conditions, and the evolving physical processes leading to downstream cell development as the squall lines approach the stable layers. Section 4 discusses the relationship between the postcollision ascent mechanisms and storm intensity, alternate processes leading to precollision downstream cell development, as well as implications for squall line sensible hazards. A summary is provided in section 5.

2. Numerical methods and data

Idealized numerical modeling offers the opportunity to isolate the impact of a MABL on squall lines in the absence of other complexities (e.g., synoptic forcing; Lombardo and Colle 2013). Storms are simulated in 3D using the Cloud Model 1 (CM1; Bryan and Fritsch 2002), with 200-m horizontal grid spacing. The vertical spacing is stretched from 50 m in the lowest 3 km to 1000 m at the 20-km model top, providing 95 vertical levels. The domain is 1000 km wide in the x direction with open radiative boundaries, and 63 km wide in the y direction with periodic boundaries. Upper and lower boundaries are free slip, with a Rayleigh damping sponge layer above 15 km. A Klemp–Wilhelmson time-splitting vertically implicit pressure solver is used, with a large time step of 0.75 s following a Runge–Kutta scheme (Klemp and Wilhelmson 1978). A fifth-order scheme with implicit diffusion is used to integrate the horizontal and vertical advection of velocities and scalars, with a weighted essentially nonoscillatory (WENO) scheme applied at the final Runge–Kutta time step to the advection of scalars (Shu 2001; Wicker and Skamarock 2002).

Storms are initiated using momentum forcing, with random fluctuations to the initial perturbation θ up to ± 2.0 K to generate 3D circulations (Morrison et al. 2015). Forcing is centered 100 km from the left boundary, with a 10-km horizontal radius, and decreases to zero by 1-h model time. Microphysical processes are calculated with the double-moment Morrison scheme (Morrison et al. 2009). Radiation and surface fluxes are not included to simplify the interpretation of the solutions (i.e., no diurnal cycle), with subgrid scale turbulence parameterized with a TKE scheme (Deardorff 1980).

a. Mid-Atlantic analytic vertical profile

The base-state analytic thermodynamic profile is based on environments observed to support squall lines in the mid-Atlantic coastal plain east of the Appalachian Mountains (Letkewicz and Parker 2010). Storms that develop in this region have the potential to, and often do, move toward the coastline and encounter the MABL. SBCAPE is 1500 J kg^{-1} with 15 m s^{-1} of vertical wind shear in the lowest 3.5 km (Fig. 1). Details are provided in the appendix.

b. MABL description

Sensitivity experiments include MABLs with different buoyancy and depth values, common characteristics used to

define a MABL. Simulations include either a 1500- or 750-m-deep MABL with a -3 - or -6 -K θ' , with perturbation values based on the adjacent ambient air. Base-state moisture is initially preserved in the marine layer when the thermal perturbation is applied. RH is therefore allowed to vary within the marine layer, leading to increased saturation in the layer. Values are informed by observed thermodynamic profiles along the coastal mid-Atlantic [e.g., Chatham, Massachusetts (CHH); Upton, New York (OKX); Wallops Island, Virginia (WAL); Newport, North Carolina (MHX)] during the warm season (June–August), previous 2D (LK18) and preliminary 3D experiments, and documentation in the literature (Keyser and Anthes 1977; Miller et al. 2003; Crosman and Horel 2010; Lombardo and Colle 2013; Nunalee and Basu 2014; Lombardo et al. 2016, 2018; LK18). A MABL depth of 1500 m reduces the low-level potential instability in the marine environment, creating thermodynamically less favorable conditions for storms; however, elevated instability is still present above the marine layer, which has been shown to help support organized storms over stable layers (Trier et al. 2006).

The MABL is inserted as a rectangular block at $t = 0$ in the right side of the domain, following LK18. Its depth decreases as the dense air spreads across the domain toward the storm. To obtain the targeted depth value at the time of collision with the storm, MABL depth is initially 2 (1) km for the 1500 (750)-m-deep experiments. The MABL “western” edge is staged to ensure the cold pool–MABL collision is near 225 min (model time) and 300 km (in the x direction) for all simulations. All storms reach maturity prior to interacting with the MABL.

3. Results

a. Precipitation evolution

The control experiment illustrates storm evolution in the absence of a MABL, and is presented as a baseline for the quantification of MABL impacts. Following initiation, convection organizes into a quasi-linear squall line, with localized regions of intense convection, as depicted by 2–7-km vertically averaged precipitation mixing ratio maxima ($q_{\text{prcp}} > 1.28 \text{ g kg}^{-1}$; Fig. 2a). Several hours after initiation (195 min), domain maximum surface rainfall rate is 140 mm h^{-1} (Table 1), total volume of precipitation mixing ratio mass $> 5 \text{ g kg}^{-1}$ ($> 3 \text{ g kg}^{-1}$) is 145 km^3 (1340 km^3 ; Table 2), with a maximum updraft velocity (w_{max}) of 33.9 m s^{-1} (Table 3). As the squall line traverses the domain, its spatial structure remains similar, as depicted by the vertically averaged q_{prcp} (Fig. 2b). Though there are small increases in surface rainfall rate (rr_{max} , 15 mm h^{-1} increase; Table 1) as well as domain total volume mixing ratio mass > 5 and $> 3 \text{ g kg}^{-1}$ (1% and 14% increase, respectively; Table 2) between 195 and 300 min, signs of weakening are apparent with a reduction in w_{max} (28.9 m s^{-1} ; Table 3) and domain total volume of w_{max} exceeding 10 m s^{-1} (21%; Table 4). By 405 min, weakening is evident in the precipitation fields (Fig. 2c), with a substantial drop in total mass within the most convectively active segments of the line. The volume of q_{prcp} mass exceeding 5 and 3 g kg^{-1} decreases 45% and 50%, respectively (Table 2). The squall line continues to

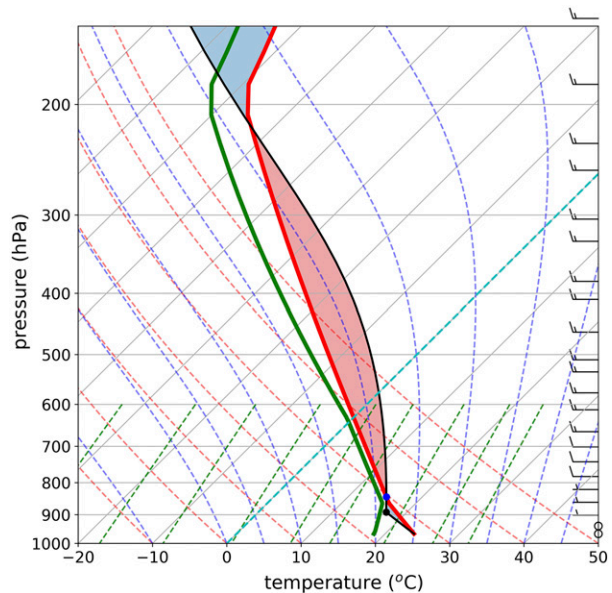


FIG. 1. Skew T –log p diagram of the analytic mid-Atlantic profile with temperature in red and dewpoint in green. The LFC is 843 hPa (blue dot) and LCL is 891 hPa (black dot). The path of a lifted surface parcel is traced in black, with CAPE (CIN) shaded in pink (blue).

weaken (Fig. 2d), with a reduction in all provided intensity metrics, and ultimately decays within the domain. Considering precipitation metrics of rainfall rate, precipitation mixing ratio mass, and rain mass (Fig. 3), this is the weakest storm of the experiments.

Storm evolutions in the presence of the MABLs are initially similar to the control (not shown); however, as the storms approach the marine layers, they intensify (Figs. 4a–7a). Considering the storm interaction with the coldest, deepest (-6 -K- θ' , 1500-m-deep) MABL, rr_{max} is 40% larger than in the absence of a MABL (Table 1), with the greatest convective precipitation mass among the experiments (Table 2). A key contributor to the increase in precipitation is the development of a 50-km-wide field of isolated cells that forms in front of and parallel to the squall line, approximately thirty minutes prior to its collision with the MABL (Fig. 4a). The development of these cells is associated with the discrete propagation of the storm as it moves toward the marine environment. The evolution of ambient conditions leading to the development of the cells and the dominant physical processes are detailed in section 3d. Domain total rain mass increases and peaks *prior* to the interaction (collision) between storm cold pool and MABL, and is largest among the experiments at this time (Fig. 3).¹

Following, the squall line reorganizes and moves over the stable layer as a linearly coherent system (Fig. 4b). By 300 min, rr_{max} is 239 mm h^{-1} , 50% greater than the control storm at this

¹ The larger total rain prior to 125 min is due to the transient precipitation associated with the insertion of the MABL.

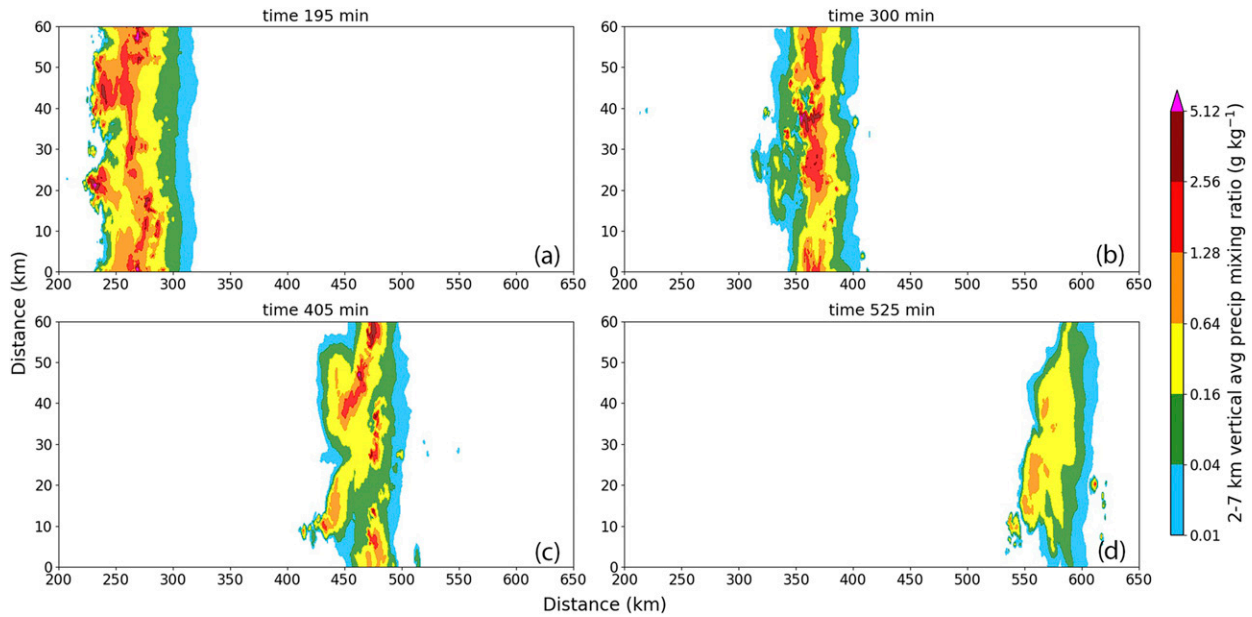


FIG. 2. Four-panel plan view of 2–7-km vertically averaged precipitation mixing ratio (g kg^{-1}) for the control experiment with no MABL at (a) 195, (b) 300, (c) 405, and (d) 525 min.

time (Table 1). Volume of $q_{\text{prcp}} > 5 \text{ g kg}^{-1}$ and $q_{\text{prcp}} > 3 \text{ g kg}^{-1}$ are 150% and 200% larger, respectively, than the control (Table 2). These increases are, in part, due to the larger volume of strong convective updrafts within the storm, with 50% more updrafts $> 15 \text{ m s}^{-1}$, 100% more updrafts $> 10 \text{ m s}^{-1}$, and a 4.3 m s^{-1} increase in w_{max} (Tables 3 and 4). Storm intensity then declines (Fig. 4c), with maximum rainfall rate and updraft velocity similar to the control storm by 405 min (Tables 1 and 3); however, the overall volume of convective updrafts and the associated precipitation remains relatively larger (Tables 2 and 4, Fig. 3). The storm remains more intense than the control storm as it continues across the domain (Fig. 4d), with more convective updrafts (Table 4), larger maximum updraft velocity (Table 3), larger rain rate (Table 1), and more total rain (Fig. 3).

When the MABL depth is halved (0.75 km, Fig. 5), new convective cells still form ahead of the primary line as the storm and MABL approach one another (Fig. 5a). Maximum rainfall and updraft velocity are slightly greater than for the

storm encountering the deep MABL (7% and 5%, respectively; Tables 1 and 3), though the volume of convective updrafts, volume of q_{prcp} , and rr_{max} are notably smaller (Tables 2 and 4, Fig. 3). Following the storm–MABL collision, evidence suggests that the squall line is initially more intense, but with smaller areas of convective activity than the storm over the deep MABL (Fig. 5b). At 300 min, total volume of stronger updrafts ($> 15 \text{ m s}^{-1}$) and higher convective precipitation mass ($q_{\text{prcp}} > 5 \text{ g kg}^{-1}$) are 38% and 13% greater, respectively; however, the volume of $q_{\text{prcp}} > 3 \text{ g kg}^{-1}$ is 30% smaller, volumes of $w > 10 \text{ m s}^{-1}$ are similar, and total rain mass is smaller (Fig. 3). Over the following several hours, the storm weakens more slowly (Figs. 5c,d), with smaller decreasing trends for all updraft and precipitation metrics than for the storm over the deep MABL.

For squall lines encountering the two less cold, $-3\text{-K-}\theta'$ MABLs, cells also form prior to the cold pool–MABL collision (Figs. 6a and 7a), though there is less convective precipitation than in the presence of their colder MABL counterparts with the same depths at this time.² Maximum rainfall is 10%–20% lower (Table 1), convective precipitation mass (both > 5 and $> 3 \text{ g kg}^{-1}$) is 60% less (Table 2), and convective updraft volume (both > 15 and $> 10 \text{ m s}^{-1}$) is 38%–46% less (Table 4), contributing to less total rain (Fig. 3).

Once over the MABLs, these relationships vary as a function time. For storms over the deep MABLs, rain rates over the $-3\text{-K-}\theta'$ MABL remain 10%–44% lower (Table 1), though precipitation mixing ratio is more variable considering both

TABLE 1. Domain maximum surface rainfall rate (mm h^{-1}). Time 1 is 195 min for the no MABL, $-6\text{-K-}\theta'$ 1500-m MABL, and $-3\text{-K-}\theta'$ 750-m MABL experiments; time 1 is 210 min for the $-6\text{-K-}\theta'$ 750-m MABL experiment and 180 min for the $-3\text{-K-}\theta'$ 1500-m MABL experiment. Time 2 is 300 min, time 3 is 405 min, and time 4 is 525 min for all experiments.

MABL	Time 1	Time 2	Time 3	Time 4
No MABL	140.0	156.3	129.0	70.6
$-6\text{-K-}\theta'$ 1500 m	194.8	239.0	122.1	73.1
$-6\text{-K-}\theta'$ 750 m	208.5	188.4	158.0	114.4
$-3\text{-K-}\theta'$ 1500 m	176.6	132.1	96.2	56.7
$-3\text{-K-}\theta'$ 750 m	164.9	145.2	141.5	94.2

²The early development of cells (180 min) in the presence of the $-3\text{-K-}\theta'$ 1.5-km-deep MABL is associated with a 10–15 min earlier collision time.

TABLE 2. Domain total volume (km^3) of precipitation mixing ratio mass greater than 5 g kg^{-1} (top row of each simulation) and 3 g kg^{-1} (bottom row of each simulation). Times as in Table 1.

Simulation	Time 1	Time 2	Time 3	Time 4
No MABL	144.8	155.1	84.6	0
-6-K- θ' 1500 m	1339.1	1529.2	769.1	0
	797.8	385.5	377.3	0
	5147.2	4547.8	4171.2	0.2
-6-K- θ' 750 m	784.5	437.3	585.3	30.6
	3518.6	3121.2	3509.2	1850.4
-3-K- θ' 1500 m	329.0	566.6	51.9	0
	3551.8	3883.1	2196.2	453.1
-3-K- θ' 750 m	324.9	174.7	819.1	119.3
	2464.3	3281.1	3539.3	1308.2

quantitative metrics and spatial distribution (Figs. 4b–d and 6b–d). Total volume of $q_{\text{prcp}} > 5 \text{ g kg}^{-1}$ is 47% larger at 300 min and $q_{\text{prcp}} > 3 \text{ g kg}^{-1}$ is nonzero at 525 min, but q_{prcp} values are smaller at other times. Maximum updraft velocity is $2.4\text{--}9.1 \text{ m s}^{-1}$ smaller and total convective updraft volume is 44%–88% less, with the exception of the stronger convective updraft volume at 525 min, when both values are effectively zero (Table 4). This combination indicates that the storm over the less cold MABL is weaker, and contributes to less total rain associated with the storm (Fig. 3).

For storms over the shallow MABLs, their relative strengths compared to one another change overtime. At 300 min, the storm over the -3-K- θ' MABL is *weaker*, with a 2.4 m s^{-1} smaller maximum updraft velocity, 66% and 46% smaller volume of $w > 15$ and $> 10 \text{ m s}^{-1}$, respectively, 22% smaller maximum rainfall rate, and 60% smaller volume of $q_{\text{prcp}} > 5 \text{ g kg}^{-1}$. Volume of $q_{\text{prcp}} > 3 \text{ g kg}^{-1}$ is 5% larger. By 405 min, however, the storm over the -3-K- θ' MABL is *more intense*, with a 3.2 m s^{-1} larger maximum updraft velocity, as well as a larger volume of the most intense updrafts and precipitation: $w > 15 \text{ m s}^{-1}$ is 35% larger and $q_{\text{prcp}} > 5 \text{ g kg}^{-1}$ is 40% larger. Volumes of $w > 10 \text{ m s}^{-1}$ and $q_{\text{prcp}} > 3 \text{ g kg}^{-1}$ are similar between the two storms at this time. By 525 min, storm intensity is more similar given variability among the metrics, with a 289% (due to changes in small values) larger volume of $q_{\text{prcp}} > 5 \text{ g kg}^{-1}$ and a 1.4 m s^{-1} higher w_{max} , though $q_{\text{prcp}} > 3 \text{ g kg}^{-1}$ (30%), maximum rainfall rate (18%), volume of $w > 15$ and $> 10 \text{ m s}^{-1}$ (54% and 46%, respectively) are smaller. For these two storms, the more intense storm (i.e., the storm over the -6-K- θ' vs -3-K- θ') changes with time and changes based on the intensity metric at a given time. Consequently, total rain

TABLE 3. Domain maximum updraft velocity (m s^{-1}). Times as in Table 1.

MABL	Time 1	Time 2	Time 3	Time 4
No MABL	33.9	28.9	27.3	12.8
-6-K- θ' 1500 m	36.4	33.2	27.6	18.0
-6-K- θ' 750 m	38.5	30.9	30.3	26.6
-3-K- θ' 1500 m	39.7	25.4	18.5	15.6
-3-K- θ' 750 m	29.2	28.5	33.5	28.0

TABLE 4. Domain total volume (km^3) of updrafts with velocity greater than 15 m s^{-1} (top row of each simulation) and 10 m s^{-1} (bottom row of each simulation). Times as in Table 1.

Simulation	Time 1	Time 2	Time 3	Time 4
No MABL	41.9	41.9	17.3	0
-6-K- θ' 1500 m	177.8	140.5	91.1	1.3
	220.6	61.2	29.6	1
	703.4	275.5	156.2	19.7
-6-K- θ' 750 m	171.5	84.0	52.3	28.2
	510.5	291.3	202.5	104.5
-3-K- θ' 1500 m	118.7	30.0	3.7	0
	416.1	155.4	51.9	3.5
-3-K- θ' 750 m	105.3	28.3	70.8	12.9
	417.2	158.4	202.0	55.7

mass for the two storms is similar (Fig. 3), suggesting little sensitivity to MABL θ' for sufficiently shallow MABLs.

Finally, two notable differences exist comparing storms engaging with a deep versus a shallow MABL. First, the pre-collision total rain peak occurs closer to the collision time for storms over shallow MABLs (Fig. 3). Sensitivity of cell development and the associated rain peak to collision timing is addressed in section 3e, and illustrates that neither are dependent on storm age. Second, at 525 min, maximum rainfall rate, maximum updraft velocity, precipitation mixing ratio volume, and updraft volume are all substantially larger for storms over the shallow MABLs, indicating a later decay time.

b. Physical processes associated with traversing the MABL

Once over the MABL, the storm precipitation evolution is dependent on the physical mechanisms that provide ascent. This will be addressed in the following sections, but only for storms interacting with two deep (1.5-km) MABLs, given that 1) differences in q_{prcp} , through visual inspection and metrics such as maximum rainfall rate, are more sensitive to MABL θ'

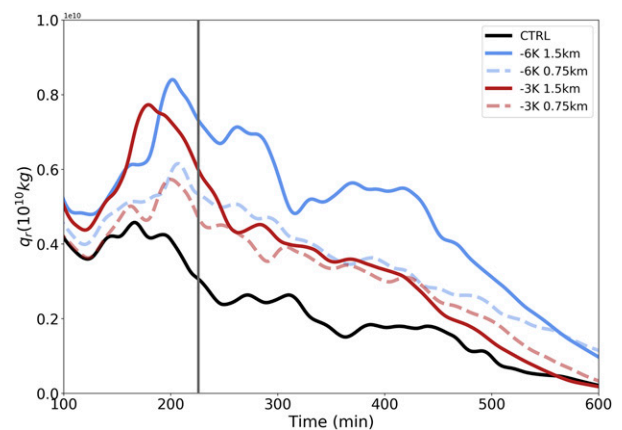


FIG. 3. Time series of the total mass of rain in the domain for the control experiment with no MABL (black), storms interacting with the 1.5- (solid) and 0.75-km (dashed)-deep -3-K- θ' MABL (red), and storms interacting with the 1.5- (solid) and 0.75-km (dashed)-deep -6-K- θ' MABL (blue). The gray line marks the approximate time of collision (225 min) between the storms and MABLs.

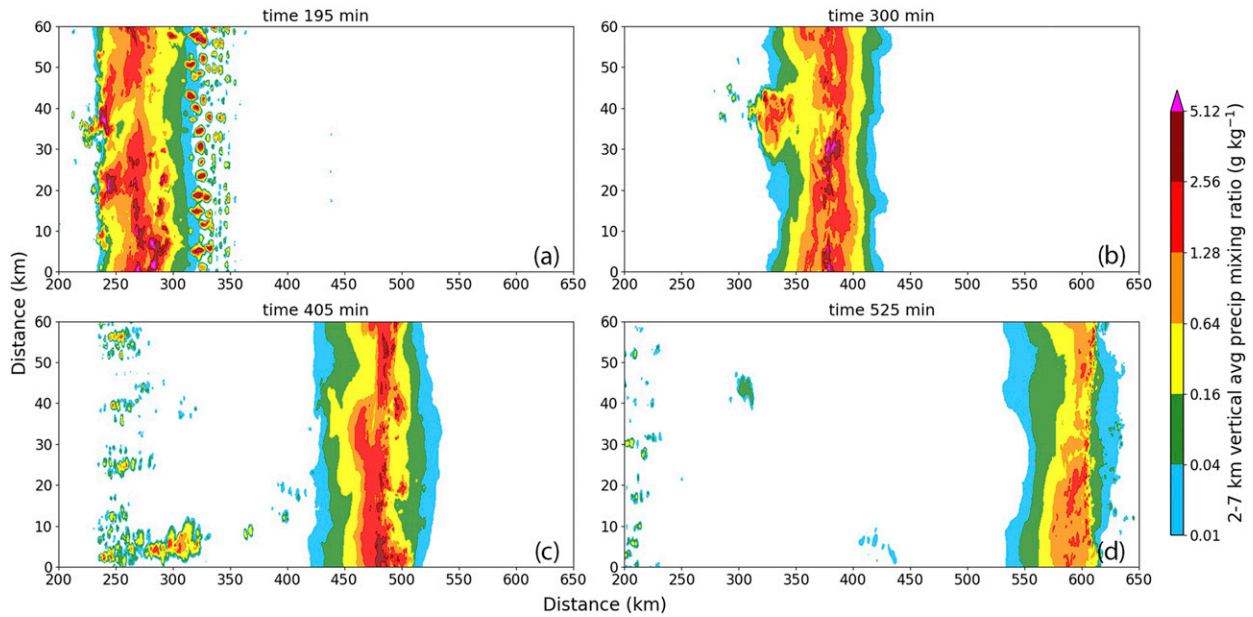


FIG. 4. As in Fig. 2, but for the storm interacting with a $-6\text{-K-}\theta'$ 1.5-km-deep MABL at (a) 195, (b) 300, (c) 405, and (d) 525 min.

than depth postcollision, and 2) the impact of MABL θ' on total rain is larger for storms over the deep MABLs.

1) BORE FORCED ASCENT

The storm ascent mechanism after the initial interaction between its cold pool and the MABL is dependent on the cold pool–MABL buoyancy relationship described in LK18. Figure 8 illustrates y -averaged cross sections of buoyancy and vertical motion before and after the storm collides with the $-6\text{-K-}\theta'$ 1.5-km-deep MABL. Buoyancy is calculated as

perturbations from the base-state environment. Prior to collision, the storm is supported by surface-based cold pool ascent as it moves from west to east. Here, the cold pool buoyancy deficit (left side of the domain) is smaller than the buoyancy deficit of the MABL (right side of the domain). This sets the stage for the transition to a new ascent mechanism following their interaction. The collision generates a bore evidenced by the characteristic periodic ascending and descending motion at and behind the storm's leading edge, and the absence of a buoyancy gradient within the lowest 1 km (Fig. 8b). The bore

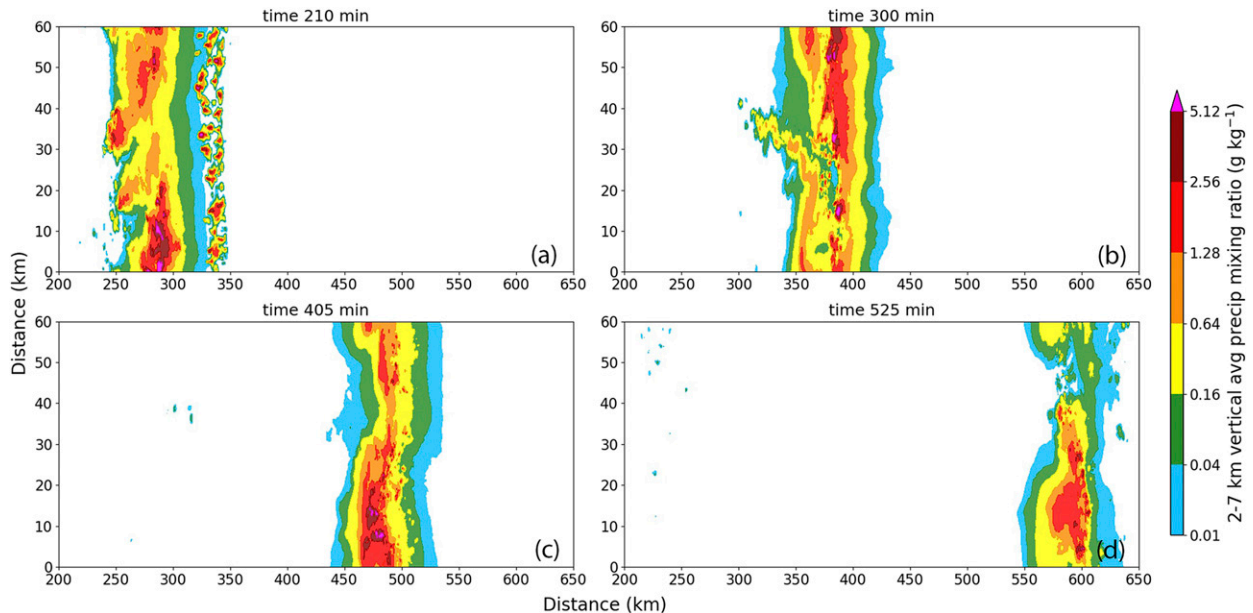


FIG. 5. As in Fig. 2, but for the storm interacting with a $-6\text{-K-}\theta'$ 0.75-km-deep MABL at (a) 210, (b) 300, (c) 405, and (d) 525 min.

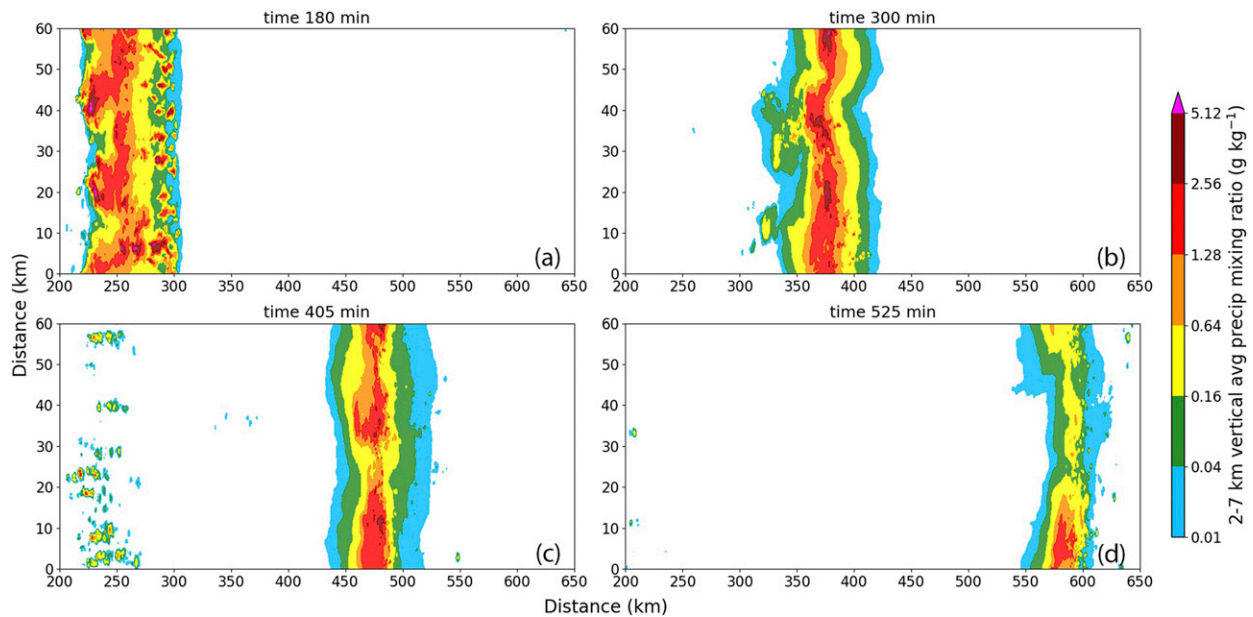


FIG. 6. As in Fig. 2, but for the storm interacting with a $-3\text{-K-}\theta'$ 1.5-km-deep MABL at (a) 180, (b) 300, (c) 405, and (d) 525 min.

serves as the source of parcel lift as it propagates along the top of the MABL (Figs. 8d,e). Parcels originating above (1500–2000 m) and within the upper portion of the MABL (500–1000 m, 1000–1500 m) rise into the storm updraft, though parcels originating from the lowest levels (surface–500 m), thus with the lowest buoyancy, remain near the surface. This bore-generated ascent is the largest of the experiments, supporting the production of the most total rain (Fig. 3). A bore also forms and provides lift for the storm interacting with the shallower, 0.75-km $-6\text{-K-}\theta'$ MABL, though the magnitude of the ascent is smaller (not shown).

Additional evidence of bore development is provided in y -averaged cross sections of total vertical acceleration, the vertical acceleration component from flow dynamics (Fig. 9a), and the vertical acceleration component from buoyancy (Fig. 9b). Decomposition of the total vertical acceleration illustrates the physical processes associated with the vertical acceleration. Patterns in these fields aid in the identification of the type of ascent mechanism associated with the acceleration. For density currents, the dynamic pressure perturbation is maximized in front of the cold pool leading edge, associated with ascent at the leading edge, while the buoyant pressure

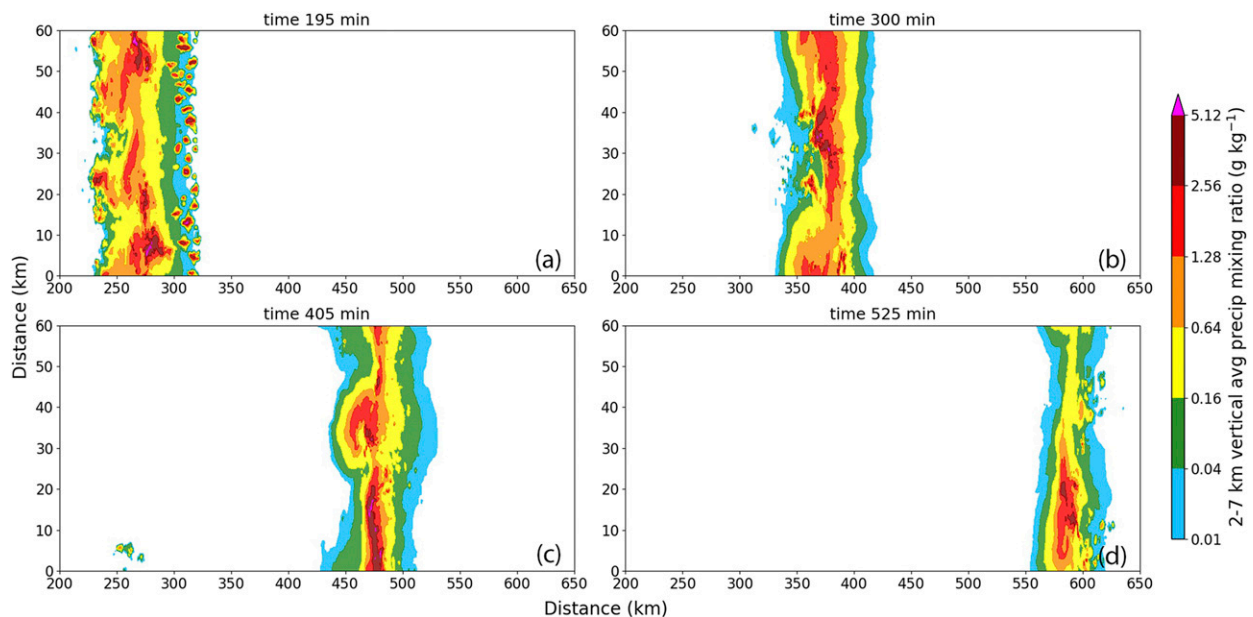


FIG. 7. As in Fig. 2, but for the storm interacting with a $-3\text{-K-}\theta'$ 0.75-km-deep MABL at (a) 195, (b) 300, (c) 405, and (d) 525 min.

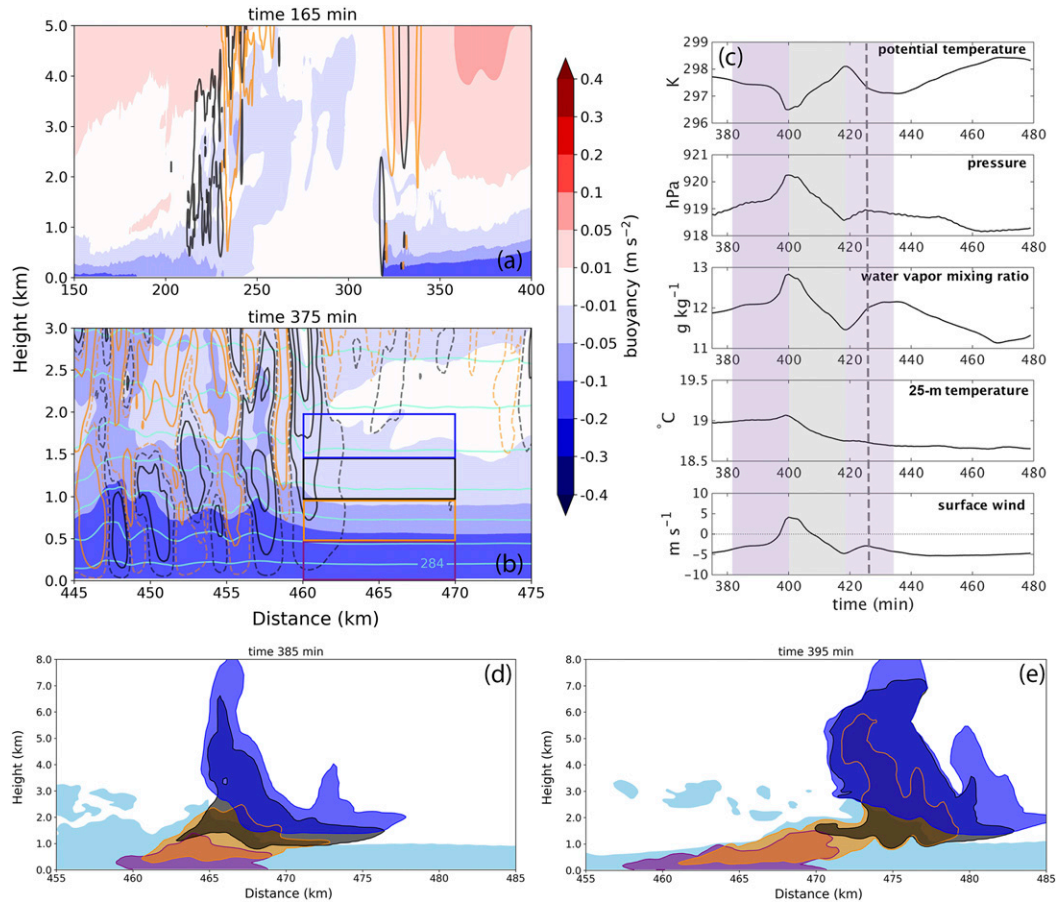


FIG. 8. Cross sections of 30–35-km y -averaged buoyancy (m s^{-2} , shaded) and vertical motion (0.5, 1.5, 3, and 6 m s^{-1} contoured black, -0.5 , -1.5 , -3 , and -6 m s^{-1} contoured orange) for the storm interacting with the $-6\text{-K}/\theta'$ 1.5-km-deep MABL at (a) 165 and (b) 375 min (includes vertical motion values of 0.1 and -0.1 m s^{-1} in dashed, and potential temperature contours every 2 K in aquamarine beginning at 284 K). Note that the horizontal domain in (b) is zoomed in to 445–475 km. (c), (top to bottom) Time series located at 480 km of 30–35-km y -averaged 500-m potential temperature ($\theta_{500\text{m}}$), 500-m pressure ($p_{500\text{m}}$), 500-m water vapor mixing ratio ($q_{v,500\text{m}}$), 25-m temperature (T_{sfc}), and surface wind (u_{sfc}). Cross sections of 30–35-km y -averaged passive tracers released at 375 min initialized between 460 and 470 km in the horizontal, and between the surface and 500 m (shaded purple), 500 and 1000 m (shaded orange), 1000 and 1500 m (shaded gray), and 1500 and 2000 m (shaded blue) in the vertical at (d) 385 and (e) 395 min, as shown in (b). Buoyancy $< -0.05 \text{ m s}^{-2}$ is shaded light blue.

perturbation is maximized behind, associated with the horizontal movement of the current. For gravity waves, an oscillatory pattern in both the dynamic and buoyant pressure perturbation fields is common. The total pressure perturbation p' in the anelastic, inviscid Lagrangian vertical momentum equation can be separated into the dynamic pressure perturbation p'_d from variations in the flow field and the buoyant pressure perturbation p'_b from variations in density,

$$\frac{Dw}{Dt} = -\frac{1}{\bar{\rho}} \frac{\partial p'_d}{\partial z} + \left(-\frac{1}{\bar{\rho}} \frac{\partial p'_d}{\partial z} + B \right), \quad (1)$$

where $\bar{\rho}$ is the base-state density (Emanuel 1994; Davies-Jones 2003; Doswell and Markowski 2004). The first term on the right-hand side of Eq. (1) is the dynamic vertical perturbation

pressure gradient acceleration (DVPPGA), the local acceleration due to the dynamic vertical perturbation pressure gradient force. The remaining terms comprise the buoyant contribution to the total vertical acceleration independent of the base state, including the local acceleration due to the buoyant vertical perturbation pressure gradient force and buoyancy B . By definition, effective buoyancy force (β) is defined as

$$\beta = \bar{\rho} \left(-\frac{1}{\bar{\rho}} \frac{\partial p'_d}{\partial z} + B \right). \quad (2)$$

Here, the buoyancy contribution to Dw/Dt is presented in units of acceleration, $\beta/\bar{\rho}$ (Jeevanjee and Romps 2015).

The oscillating pattern of positive and negative total vertical acceleration within the lowest 1 km echoes patterns in vertical

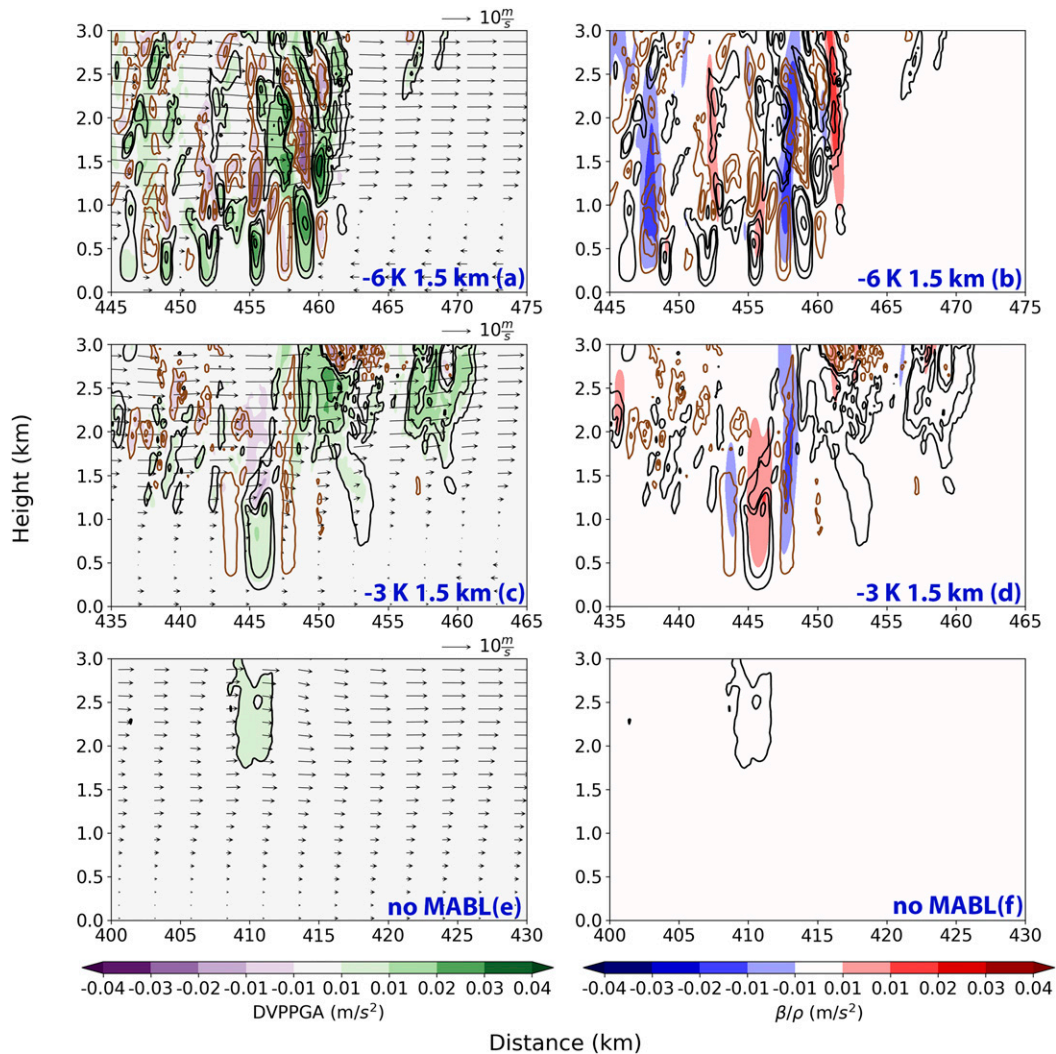


FIG. 9. Cross sections of total vertical acceleration (0.005, 0.01, 0.02, 0.03, and 0.04 m s^{-1} contoured black; -0.005 , -0.01 , -0.02 , -0.03 , and -0.04 m s^{-1} contoured brown), plotted with (left) dynamic vertical perturbation pressure gradient acceleration (positive values shaded green, negative values shaded purple) and (right) effective buoyancy (positive values shaded red, negative values shaded blue), for storms interacting with the (a),(b) $-6\text{-K-}\theta'$ 1.5-km-deep MABL at 375 min, (c),(d) $-3\text{-K-}\theta'$ 1.5-km-deep MABL at 375 min, and (e),(f) no MABL at 360 min. Calculation methods follow LK18.

motion field. The contribution from the DVPPGA to the total field is clear, with the magnitude and location of both aligned through much of the bore. Buoyancy-related physical processes are critical as well, especially within an elevated region (0.5–3.0 km) at the storm leading edge (462 km). Here, positive β associated with the approaching ridge dominates the total vertical acceleration, followed by the complementary negative acceleration associated with the trough. Behind this leading edge and within the lowest 1 km, the role of β is smaller.

Bore passage is also evident in y -averaged time series of elevated (500-m θ , 500-m pressure, 500-m q_v) and surface (temperature, wind) variables (Fig. 8c). Analysis begins at 375 min and is located at $x = 480 \text{ km}$, to capture the wave featured in the vertical motion and acceleration fields (Figs. 8 and 9).

Advancement of the initial ridge is indicated by a decrease in $\theta_{500\text{m}}$, an increase in $p_{500\text{m}}$, $q_{v-500\text{m}}$, and T_{sfc} , and a shift to westerly u_{sfc} over a 20-min period (purple shading). By 400 min, the ridge peak is located over the reference point, as variables reach their maximum or minimum values. Over the following 20 min (400–420 min), trough passage exhibits the opposite trend: an increase in $\theta_{500\text{m}}$, a decrease in $p_{500\text{m}}$, $q_{v-500\text{m}}$, and T_{sfc} , and a shift to easterly u_{sfc} (gray shading).

After 420 min, trends initially show the next approaching wave crest (purple), though only for 5 min. Instead, easterly surface winds intensify, $p_{500\text{m}}$ decreases, and the rate of change in $\theta_{500\text{m}}$ and $q_{v-500\text{m}}$ is dampened (dashed line). This change may signal the smaller amplitude and period of an approaching second wave, with trends illustrating the muted reflection of the

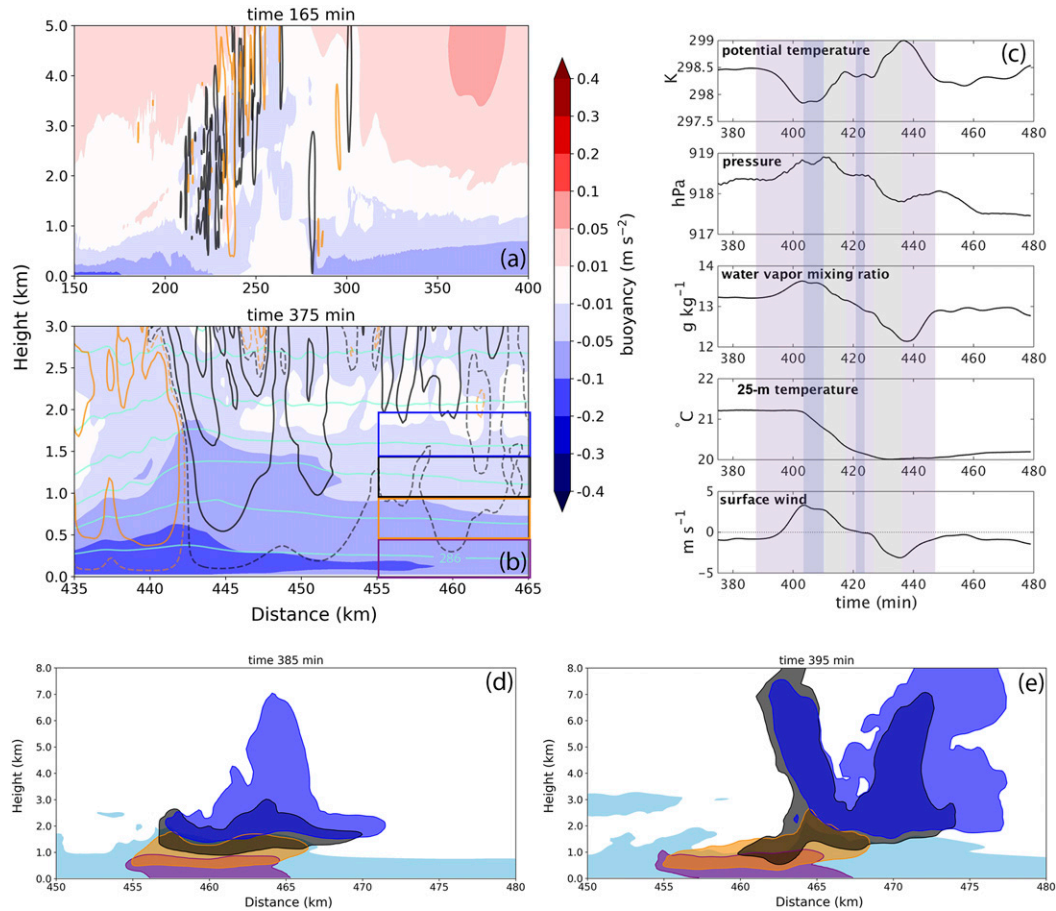


FIG. 10. As in Fig. 8, but for the storm interacting with a $-3\text{-K-}\theta'$ 1.5-km-deep MABL. Potential temperature contours begin at 286 K. (b) The horizontal domain is zoomed in to 435–465 km. Passive tracers are released at 375 min initialized between 455 and 465 km in the horizontal.

trough. Perhaps, however, this is the passage of the storm cold pool, with an increase in $p_{500\text{m}}$ and $q_{v-500\text{m}}$, a decrease in $\theta_{500\text{m}}$, a subtle decrease in T_{sfc} , and a relaxed easterly u_{sfc} . Regardless of the feature, each is convolved with the advancement of the MABL, marked by a sustained easterly u_{sfc} component.

2) COLD POOL–BORE HYBRID FORCED ASCENT

For the storm interacting with the less cold MABL, the buoyancy of the cold pool and MABL are similar (Fig. 10). In this regime, the cold pool–MABL collision results in a feature that is neither a clear cold pool nor bore. Rather, a cold pool–bore hybrid develops. A broad, weak ascent–descent couplet marks the leading edge of the storm, indicative of vertical motion associated with a cold pool; however, there is evidence of embedded bore motion. Within the broad region of ascent are two distinct maxima located near 450 and 445 km, with a relative minimum in vertical motion between. Similarly, two lobes are present within the broad region of descent, centered at 440 and 435 km. The alternating enhancements and weaknesses within the larger region of ascent–descent suggest that vertical motion associated with a cold pool and bore are superposed. Initially, air above the stable layer (1500–2000 m)

rises in response to the leading ascent maxima (Fig. 10d), while air within the MABL (500–1500 m) ascends in response to the second ascent maximum (Fig. 10e). A hybrid feature forms following the collision with the shallower, 0.75-km, $-3\text{-K-}\theta'$ MABL as well. Ascent–descent structures are similar, though narrower horizontally and shallower vertically, and smaller in magnitude (not shown).

A similar superposition is evident in the vertical acceleration fields. One primary region of positive acceleration is located at the leading edge of the storm between 445 and 447 km, a feature typically associated with cold pool–forced ascent (Fig. 9c); however, both the DVPPGA and β contribute to this maximum equivalently, unlike cold pool forced ascent (Fig. 9d). Further, two areas of smaller negative acceleration flank the main region of positive acceleration, both of which are dominated by buoyancy processes. Therefore, there is evidence of acceleration associated with a cold pool and a bore. For comparison, note that the bore signal is more obvious for the storm over the $-6\text{-K-}\theta'$ MABL, and there is little evidence of a single primary region of acceleration. Smaller values of vertical motion and acceleration for the storm over the $-3\text{-K-}\theta'$ MABL are consistent with the smaller rain mass totals (Fig. 3).

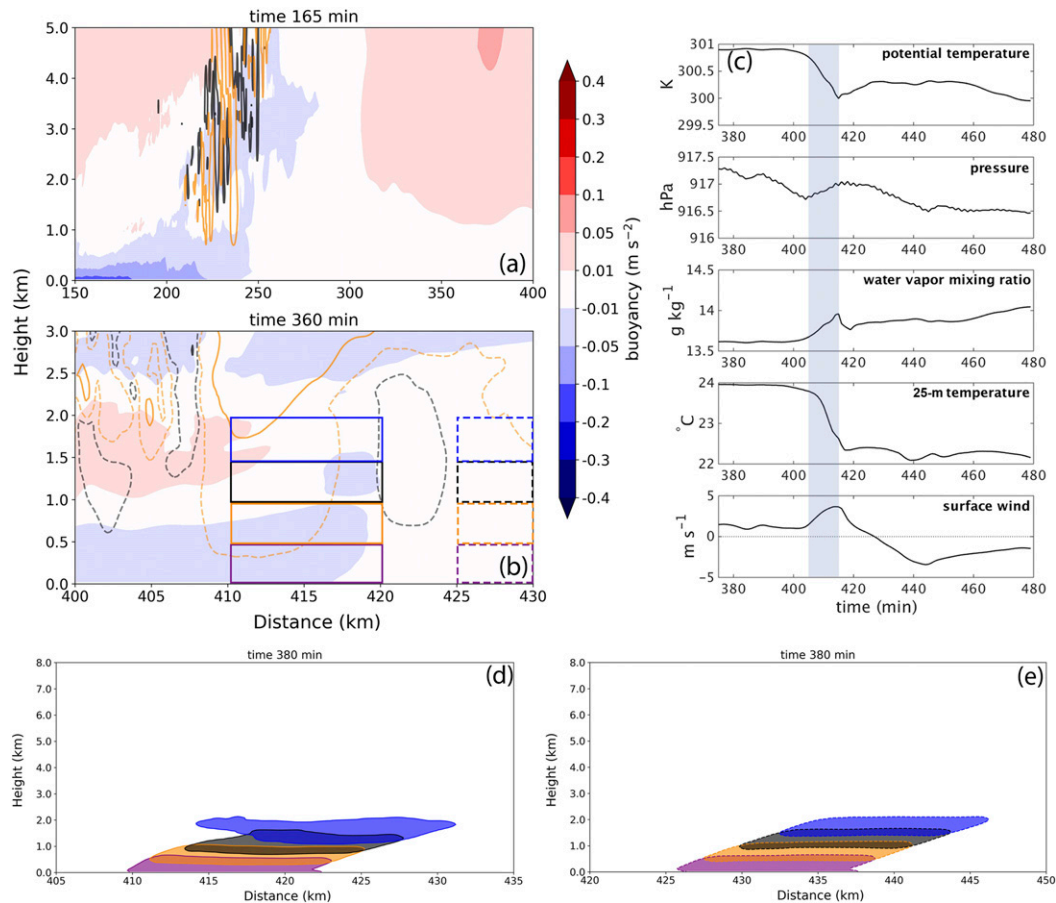


FIG. 11. As in Fig. 8, but for the control experiment with no MABL included at (a) 165 and (b) 360 min. Passive tracers are released at 360 min initialized between (d) 410–420 km (solid lines) and (e) 425–435 km (dashed lines) in the horizontal, with their location shown at 380 min only.

Passage of this hybrid feature leads to a complex time series evolution (Fig. 10c). If the passage of a cold pool boundary is defined by a decrease in $\theta_{500\text{m}}$, a gust front moves over the location between 395 and 405 min, complemented by an increase in $p_{500\text{m}}$, $q_{v-500\text{m}}$, and westerly winds at the surface (purple shading); however, T_{sfc} does not decrease as one would expect, but remains constant. Considering the passage of bore instead, trends in the variables show an approaching ridge from 395 to 405 min, except for T_{sfc} , which is expected to increase. If both are present simultaneously (i.e., hybrid), their combined and competing influence could cause T_{sfc} to remain unchanged, which is likely the case here. For completeness, if the passage of a cold pool is defined by a decrease in T_{sfc} , the gust front arrives at 405 min, though there is little evidence of this in other variables.

On the back side of the hybrid cold pool–bore ridge, there are small amplitude fluctuations in $\theta_{500\text{m}}$ (e.g., increase then decrease in $\theta_{500\text{m}}$), $p_{500\text{m}}$, $q_{v-500\text{m}}$, and u_{sfc} , with trends indicative of a higher-frequency, smaller-amplitude trough–ridge wave couplet (405–410 min, blue shading). Subsequently, the larger-amplitude, lower-frequency trough

(and complement to the ridge) passes over between 410 and 418 min (gray shading). After, there is again evidence a higher-frequency, smaller-amplitude wave (418–425 min, blue shading) embedded within a second larger-amplitude, lower-frequency ridge (purple shading). The associated trough (425–437 min, gray) and then a third lower-frequency wave ridge (438–447 min, purple) follow, ending the passage of the hybrid feature. This evolution shows that gravity waves within the hybrid feature can have multiple frequencies. For other hybrid forced storms, the details of such a complex time series will vary, though the fundamental integration of both a cold pool and bore in the variable signals will remain.

3) COLD POOL FORCED ASCENT

In the absence of a MABL, forcing for ascent remains a cold pool, as expected (Fig. 11), with notably weaker vertical motion than for storms over the marine layers, leading to the precipitation trends. At 165 min, the buoyancy and vertical motion fields resemble those of the other experiments prior to the MABL interaction at this same time (Fig. 11a). By 360 min, the vertical motion and the buoyancy perturbations are much

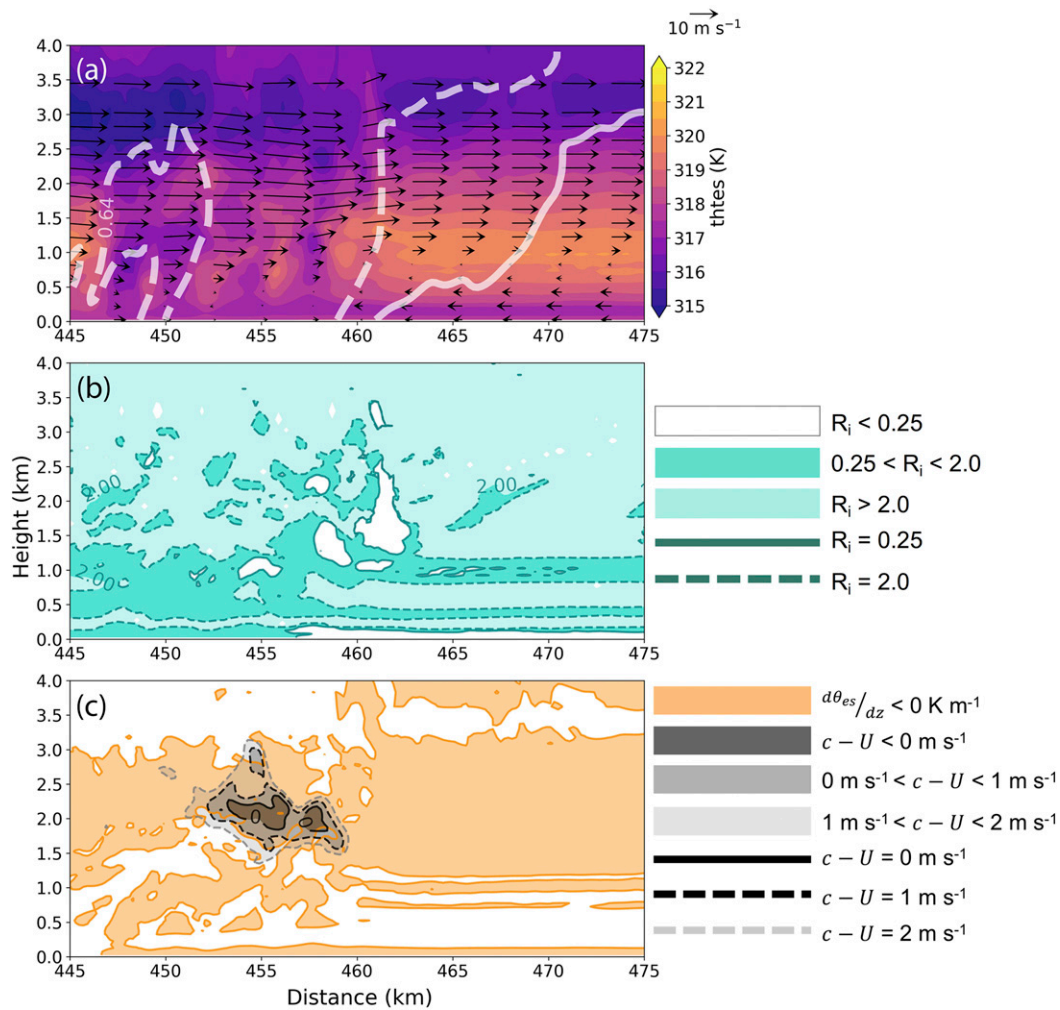


FIG. 12. Cross sections following the collision with a $-6\text{-K}\theta'$ 1.5-km-deep MABL at 375 min of 30–35-km y -averaged (a) θ_{es} (K, shaded), wind vector arrows, and precipitation mixing ratio (0.16 g kg^{-1} contoured solid gray, 0.64 g kg^{-1} contoured dashed gray); (b) gradient Richardson number (unitless, 0.25 isoline contoured solid teal, 2.0 isoline contoured dashed teal, $R_i < 0.25$ shaded white, $0.25 < R_i < 2.0$ shaded dark teal, $R_i > 2$ shaded light teal); and (c) $d\theta_{es}/dz < 0 \text{ K m}^{-1}$ (shaded orange), $c - U < 0 \text{ m s}^{-1}$ (shaded black), $0 < c - U < 1 \text{ m s}^{-1}$ (shaded dark gray), $1 < c - U < 2 \text{ m s}^{-1}$ shaded light gray, 0 m s^{-1} contoured solid black, 1 m s^{-1} contoured dashed black, and 2 m s^{-1} contoured dashed gray.

smaller, and the storm updraft appears to have split (Fig. 11b).³ One portion is located at the edge of the weakening cold pool (420–425 km), downstream of the main convective storm. Another is more elevated and collocated with the convective line (405–410 km). This second region of ascent is the primary forcing for the decaying storm, associated with dynamically driven small positive vertical acceleration (Figs. 9e,f). Passive tracers released immediately downstream of both the elevated (Fig. 11d) and surface-based (Fig. 11e) ascent illustrate that air

is no longer being ingested into the decaying storm at this time. Time series illustrate the cold pool passage as it surges ahead of the storm (Fig. 11c). The gust front moves over the location between 405 and 415 min, evidenced by a decrease in $\theta_{500\text{m}}$ and T_{sfc} , an increase in $p_{500\text{m}}$ and $q_{v-500\text{m}}$, and an increase in westerly winds (blue shading). Comparison to the time series of the hybrid feature further emphasizes that it is not strictly a cold pool (Fig. 10).

c. Environments supporting the bore and hybrid feature

For the bore to serve as the lifting mechanism for the squall line over the marine layer, a wave duct is needed to prevent the wave energy from vertically propagating away. Requirements for internal wave ducting are thought to include 1) a near-surface or surface-based stable layer to serve as a waveguide,

³ Buoyancy and ascent fields are presented for an earlier time (360 min) primarily to illustrate features sooner in the weakening phase before the storm decays.

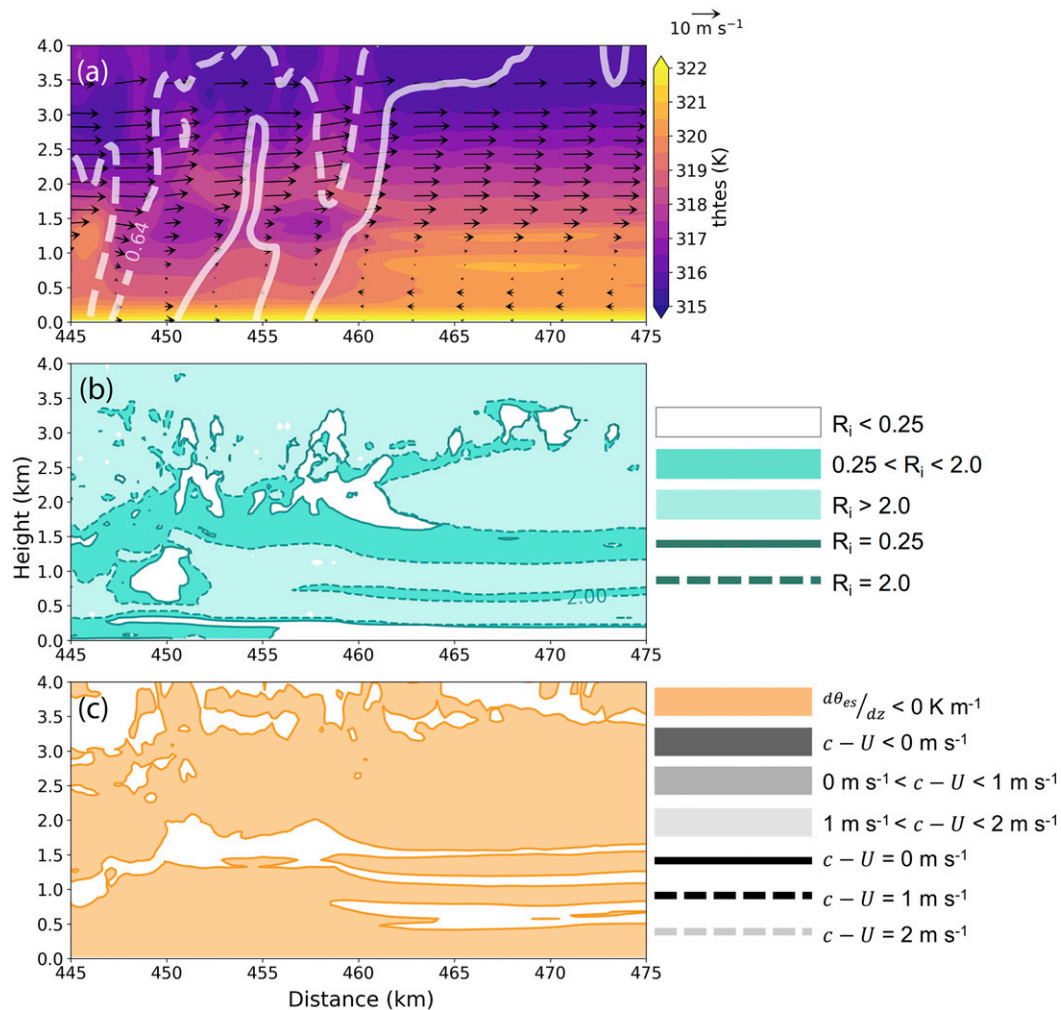


FIG. 13. As in Fig. 12, but for the storm colliding with the $-3\text{-K-}\theta'$ 1.5-km-deep MABL.

2) an overlying neutrally stable or unstable layer to serve as a reflecting layer, and 3) a critical level (i.e., where the wave ground-relative phase speed c and direction are similar to the mean flow U) embedded within the unstable layer, as a critical layer within the stable wave duct would lead to the absorption of the wave (Lindzen and Tung 1976; Crook 1988; Kingsmill and Crook 2003; Ruppert and Bosart 2014). In the presence of a critical level, wave ducting may occur for a range of Richardson number (R_i) values (a measure of dynamic instability) within the unstable layer. A large fraction of the wave energy can be reflected for $0.25 < R_i < 2$, rather than being transmitted through or absorbed by the critical level (Breeding 1971; Wang and Lin 1999). Further, gravity waves are thought to be composed of a number of wave modes with differing phase speeds, which supports the presence of a critical layer rather than a critical level (Lin 2007). Consequently, $c - U = 0 \text{ m s}^{-1}$ may not be a rigid requirement, and values near zero may suffice. This is especially true for waves in the presence of convection. Convection may alter characteristics of the environment and the local gravity waves, impacting both the mean

flow and wave phase speed. Further, given that c is typically calculated as a temporal average, both c and $c - U$ will be sensitive to the time over which the average is performed. Large vertical wind shear has also been shown to favor trapping of low-level internal wave energy (Doviak and Ge 1984; Crook 1986, 1988; Fulton et al. 1990; Fovell et al. 2006). The presence of a jet within the stable layer, which opposes wave motion and produces a reversal of wind direction between the stable layer and the overlying atmosphere (i.e., a region of curvature) can trap wave energy (Crook 1988).

Figures 12–14 illustrate that conditions are present to support internal gravity wave (bore) ducting for the storm over the coldest MABL, and conditions limit or prevent gravity wave maintenance for the storms over the less cold and no MABL. For the storm over the $-6\text{-K-}\theta'$ 1.5-km-deep MABL, the downstream environment favors gravity wave ducting (Fig. 12). The conditionally stable layer in the lowest 1 km ($d\theta_{\text{es}}/dz > 0 \text{ K m}^{-1}$) associated with the MABL serves as the waveguide, bounded by a conditionally unstable layer above from 1 to 3.5 km ($d\theta_{\text{es}}/dz < 0 \text{ K m}^{-1}$; Figs. 12a,c). Within the

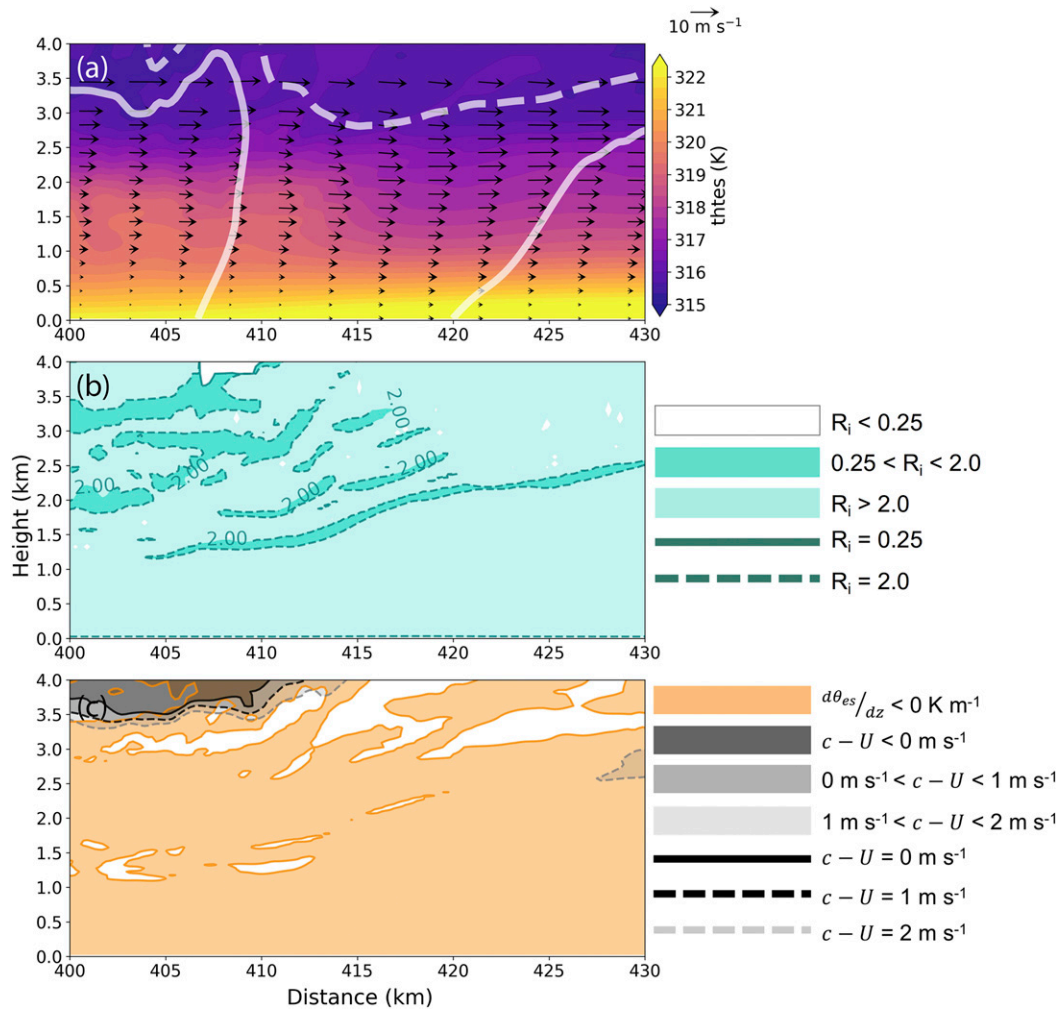


FIG. 14. As in Fig. 12, but at 360 min for the control experiment with no MABL.

unstable layer near the storm (458–464 km), $0.25 < R_i < 2$ between 1 and 2 km, which supports wave reflection (Fig. 12b). As discussed above, the determination of the $c - U = 0$ criteria depends on the value of c , which can vary in time and on the calculation method. As such, the sensitivity of this condition is tested by calculating the phase speed for different time intervals between 300 and 450 min, using several variables to track the squall line leading edge, including precipitation mixing ratio with threshold values of 0.04 and 0.16 g kg^{-1} , buoyancy with threshold values of -0.05 m s^{-2} and -0.1 m s^{-2} , as well as potential temperature $< 297 \text{ K}$. Postcollision values of c range between 15.7 and 17.6 m s^{-1} . For this analysis, a phase speed of 17.6 m s^{-1} is used, yielding the most conservative estimate of regions with $c - U = 0 \text{ m s}^{-1}$ (i.e., larger phase speeds yield smaller/fewer regions of $c - U = 0 \text{ m s}^{-1}$). Between 450 and 460 km, $c - U$ approaches zero between 1.5 and 2.5 km in height, indicating that a critical layer may be present in the unstable layer where $0.25 < R_i < 2$ (Fig. 12c). Further, the critical layer is horizontally collocated with the region of oscillating vertical motion and acceleration associated with the

bore presented in Figs. 8 and 9. Given that the region of $c - U = 0$, $0.25 < R_i < 2$, and the trapped waves are in such close proximity to the storm, one could hypothesize that the storm helps to trap the waves through modification to the vertical wind shear. Immediately ahead of the storm ($>460 \text{ km}$), a low-level jet associated with the MABL leads to an increase in vertical wind shear, which may also trap wave energy in the vicinity of the storm.

For the storm over the $-3\text{-K-}\theta'$ MABL, several of the conditions necessary to support wave trapping are marginal or not present: 1) stability in the lowest 1-km is marginal, and 2) a critical layer is absent (largest postcollision $c = 17.3 \text{ m s}^{-1}$; Fig. 13). Regardless, a hybrid feature develops. We hypothesize that perturbations to the stable layer from above due to storm downdrafts may support the continuous development of weak gravity waves (e.g., Fovell et al. 2006), but the environment cannot support their movement away from the source region. Therefore, the waves remain collocated with the generation of the cold pool.

For completeness, a similar analysis is presented for the control experiment with no MABL. A low-level stable

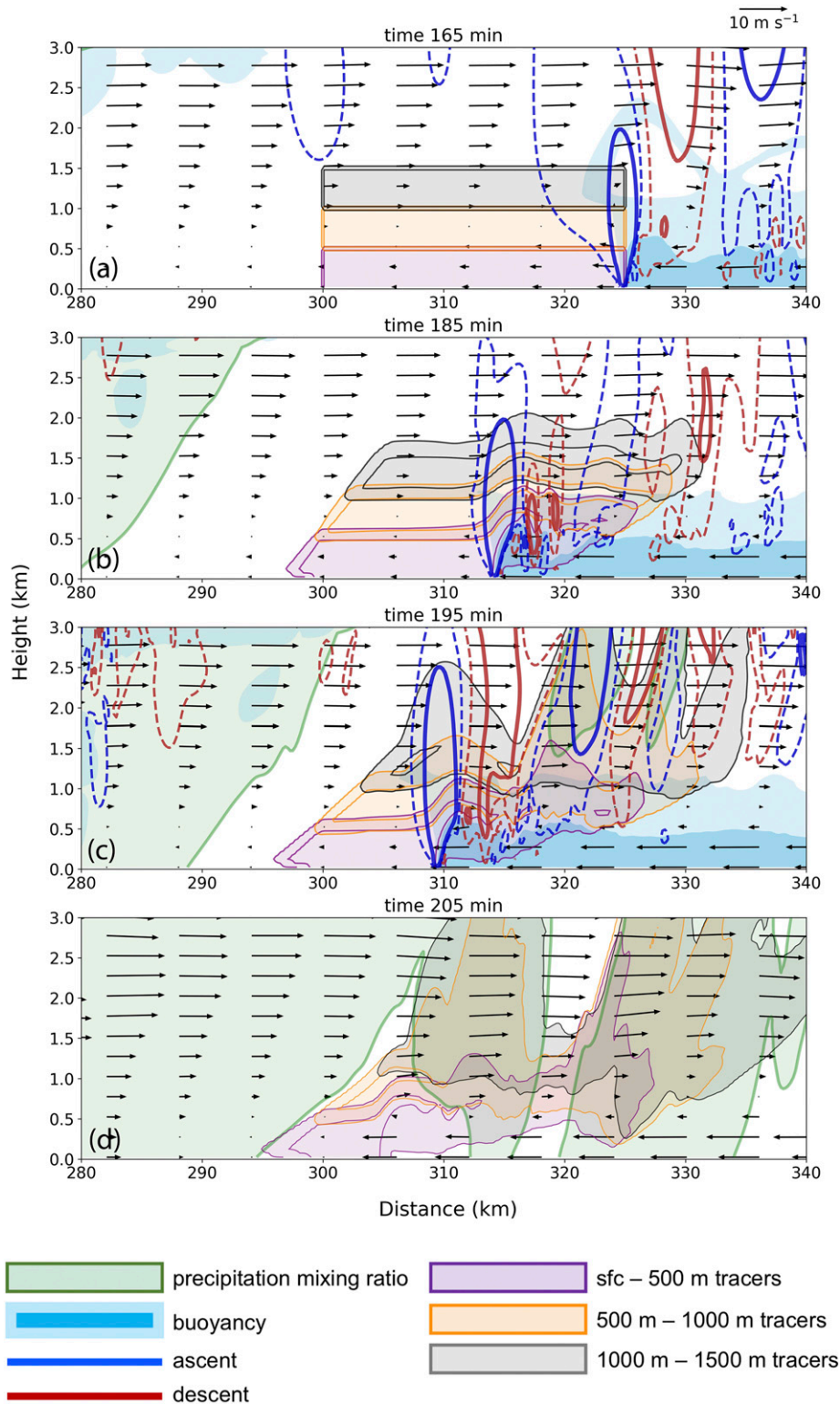


FIG. 15. Cross sections of the experiment with a $-6\text{-K-}\theta'$ 1.5-km-deep MABL of 30–35-km y -averaged passive tracers released between the surface and 500 m (shaded purple, 100% and 10% intervals contoured purple), between 500 and 1000 m (shaded orange, 100% and 10% intervals contoured orange), and between 1000 and 1500 m (shaded gray, 100% and 10% intervals contoured black), buoyancy ($-0.05 < B < -0.01 \text{ m s}^{-2}$ shaded light blue, $B < -0.05 \text{ m s}^{-2}$ shaded dark blue),

layer, favorable R_i values, and a critical layer are all absent (Fig. 14).

d. Physical mechanisms surrounding precollision cell development

The precipitation maxima that form prior to the collision between the storm cold pools and MABLs (Fig. 3) are associated with generation of cells ahead of the primary storm systems (Figs. 4–7). The development of these isolated cells illustrates the initial stages of the discrete propagation of the squall lines as they encounter the marine layers. These cells organize into the new leading edge of the storm (not shown). Here, we describe the evolving ambient conditions that lead to cell development, and present evidence that the source of these cells is the conjunction of modifications to the environment by the storm and marine layer. For consistency, this analysis highlights storms interacting with the two deep marine layers. As the coldest, deepest MABL moves across the domain, air parcels in front of the density current are initially lifted, but descend as they move over the MABL (Figs. 15a,b). A weak alternating ascent–descent pattern generated by the MABL causes air parcels to vertically oscillate with minimal displacement (<1 km). Their vertical displacement increases as the storm and the MABL approach one another. Once the two are 20 km apart, the vertical motion amplifies, precipitating convective cells form (Fig. 15c), and air parcels rise into the developing cells (Fig. 15d).

Previous studies have documented the development of isolated convective cells downstream of preexisting squall lines (Thorpe et al. 1982; Fovell et al. 2006). Cells have been shown to develop in association with convectively generated gravity waves that form in response to latent heating originating from the primary squall line, in observations (Bosart and Seimon 1988; Lin and Goff 1988) and numerical simulations (Fovell et al. 1992, 2006; LK18). The gravity waves generated comprise a broad range of frequencies (Alexander and Holton 2004), with different wavelengths and spectra, each modulating the environment uniquely. Low-frequency waves (“ $n = 2$ ”; Nicholls et al. 1991) produce ascent in the lower troposphere, which cools and moistens the atmosphere, brings it closer to saturation, and creates a more favorable environment for convection (Nicholls et al. 1991; Fovell 2002; Fovell et al. 2006). Cell triggering is attributed to the transient high-frequency waves, which are continuously generated in response to temporal fluctuations in storm latent heating (Fovell et al. 2006). For these waves to support the development of downstream cells, they need to be prevented from vertically propagating into the stratosphere (Fovell et al. 1992; Alexander and Holton 2004), with conditions necessary for wave ducting presented above.

In this study, conditions are favorable to prevent the convectively generated, high-frequency gravity waves from propagating into the stratosphere. For the $-6\text{-K-}\theta'$ MABL experiment, a reference location of 310–330 km is used in the following discussion given that new cells initiate in this longitudinal band. At 145 min, the environment at the reference location is minimally impacted by both the storm and the MABL (Fig. 16a). Conditional instability is present below 5 km with conditional stability above. The instability is enhanced closer to the storm (280–300 km) due to a band of lower θ_{es} that forms near 5 km in height immediately ahead of the storm, which may be a consequence of low-frequency, storm-generated gravity waves. As the squall line moves across the domain, so does the associated enhanced instability. Over the following 40 min, the environment at the reference location is modified by both the storm and MABL (Figs. 16b,c). The layer of conditional instability intensifies, descends, and compresses to 1–4 km, as the height of the θ_{es} minimum band decreases to 4 km and the MABL increases the stability below 1 km. Consequently, the environment becomes more favorable for convection from 1 to 4 km, and within <10 min, cells form in this layer (Fig. 16d).

Perhaps more striking is the tropospheric static stability evolution above 4 km. The initially unmodified environment at 320 km is statically stable, with $N^2 > 1 \times 10^{-4} \text{ s}^{-2}$ (saturated or subsaturated where appropriate) through a majority of the troposphere and a decrease to $0.5 \times 10^{-4} \text{ s}^{-2}$ near the tropopause (Fig. 17a). As the storm approaches this location, upper-tropospheric static stability decreases. A layer of reduced N^2 forms near 11 km and expands downward, reaching 7 km by 195 min, with minimum values below $0.25 \times 10^{-4} \text{ s}^{-2}$. Concomitantly, static stability increases between 4 and 7 km. This unstable over stable vertical configuration helps trap storm-generated gravity waves. Note, static stability decreases below 4 km, corresponding to the layer of conditional instability discussed above.

Spatial variations in N^2 at a single time (195 min) highlight the storm’s role in the tropospheric stability change (Fig. 17b). Near the storm (300 km), the layer of low stability extends from 7 to 11 km in height, but gradually contracts to 8–11 km farther away over the MABL (360 km). Once sufficiently far from the storm, tropospheric stability is restored. Such vertical variations in N^2 , with similar magnitudes, have been shown to help trap squall line-generated waves in the troposphere (e.g., Fovell et al. 2006; Nicholls et al. 1991).

The change in stability appears to be the combination of latent heating and cooling associated with the advancing storm. As the upper portion of the storm approaches the area of interest, the associated warming, centered near 8 km, destabilizes the layer above and stabilizes the layer below. The advancing storm anvil and decreasing cloud base is evident in the evolving precipitation mass fields (Figs. 16b,c), and the vertical profile of

←

vertical motion (-0.5 m s^{-1} solid red, -0.15 m s^{-1} dashed red, 0.15 m s^{-1} dashed blue, 0.5 m s^{-1} solid blue), precipitation mixing ratio ($q_{\text{precip}} > 0.04 \text{ g kg}^{-1}$ shaded green, 0.04 g kg^{-1} contoured dark green) at (a) 165, (b) 185, (c) 195, and (d) 205 min. Buoyancy and vertical motion are not included at 205 min.

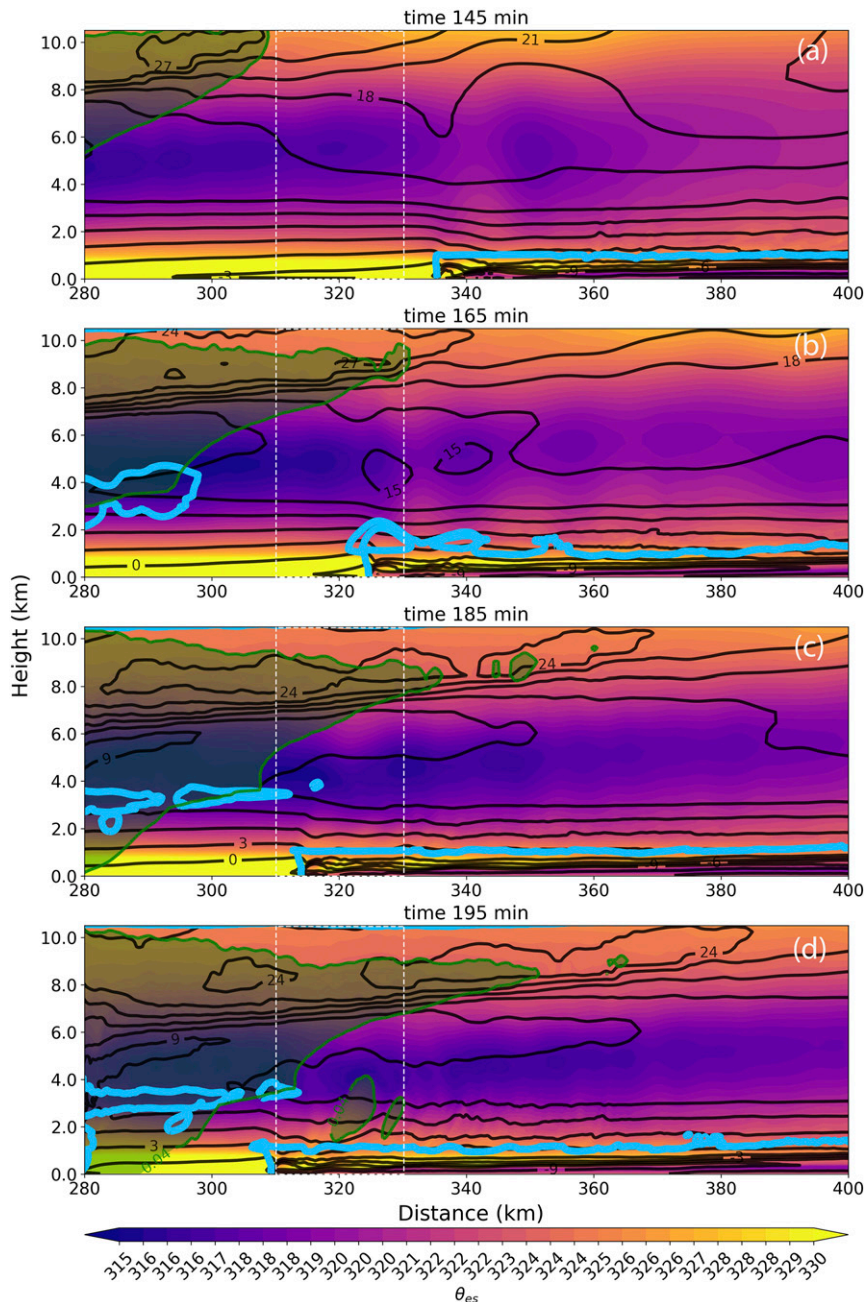


FIG. 16. Cross sections of the experiment with a $-6\text{-K-}\theta'$ 1.5-km-deep MABL of 30–35-km y-averaged saturation equivalent potential temperature (K, shaded), u wind (contoured black every 3 m s^{-1}), precipitation mixing ratio (0.04 g kg^{-1} contoured green with larger values shaded green), and buoyancy (-0.01 m s^{-2} contoured blue) at (a) 145, (b) 165, (c) 185, and (d) 195 min. White dashed box highlights the area of interest.

RH as a descending nose of increasingly higher RH between 6 and 10 km (Fig. 17c).⁴ Spatial variations in RH illustrate this as well, with a reduction in RH between 6 and 10 km moving from

⁴ RH with respect to ice is maximized between 11 and 12 km and hovers near 85%–90%.

west to east (Fig. 17d). Evaporative cooling underneath the anvil may also contribute to the increase in 4–7-km stability (Parker and Johnson 2004). A layer of negative buoyancy forms at the interface between the anvil base and clear air below between 3 and 4 km (Figs. 16b,c), accompanied by an increase in RH below 4 km, suggesting that diabatic cooling is maximized at this level. This may also contribute to the

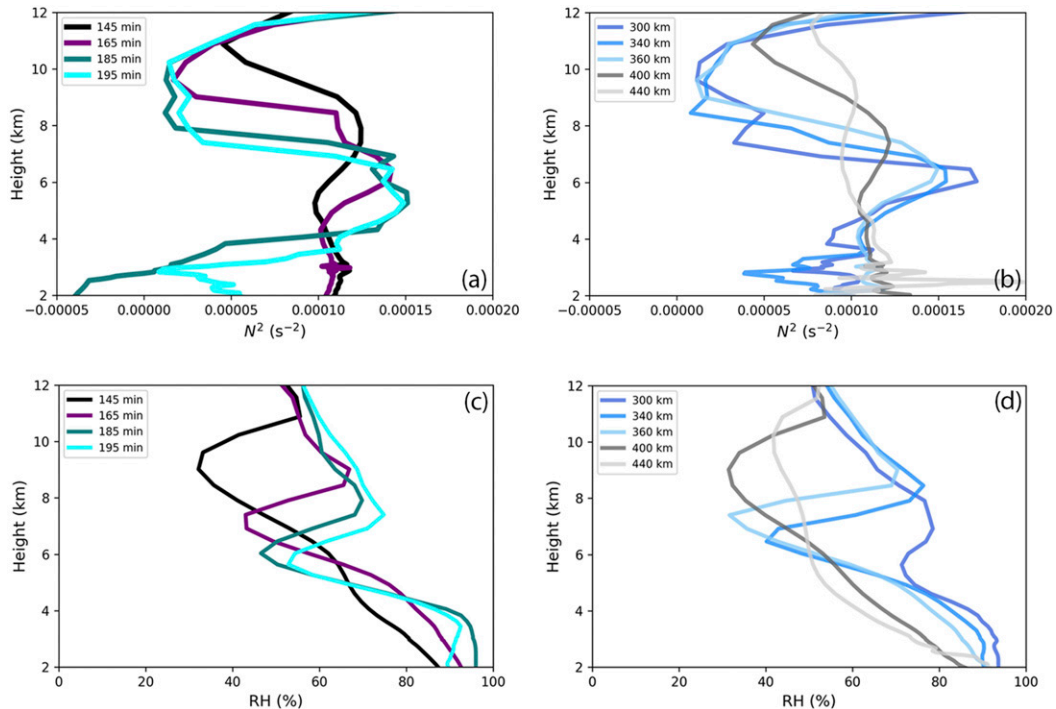


FIG. 17. Vertical profile from the experiment with a $-6\text{-K-}\theta'$ 1.5-km-deep MABL of 30–35-km horizontally y-averaged Brunt–Väisälä frequency squared (s^{-2} ; saturated or subsaturated where appropriate) (a) located at 320 km at 145 (black), 165 (purple), 185 (teal), and 195 min (cyan), and (b) at 195 min located at 300 (dark blue), 340 (blue), 360 (light blue), 400 (dark gray), and 440 km (light gray). (c) As in (a), but for relative humidity (RH, %) with respect to water. (d) As in (b), but for relative humidity (RH, %) with respect to water.

generation and descent of the layer of reduced θ_{es} , as the anvil base descends as the storm approaches.

In the presence of a favorable vertical stability profile, it has been shown that enhancements in upper-tropospheric winds due to a storm's anvil outflow creates a critical layer in the unstable layer sufficient to trap the storm's own gravity waves (Fovell et al. 2006). The outflow jet can increase the environmental wind to match the gravity wave phase speed, and at times can cause a reversal in wave-relative wind direction. For our storm, the precollision squall line-generated gravity waves propagate at an estimated 22 m s^{-1} (not shown). Therefore, the outflow-enhanced jet speed of $>24\text{ m s}^{-1}$ between 7 and 10 km allows $c - U$ to approach, and likely fall below (i.e., wind reversal) zero in the layer of reduced static stability (Fig. 16).

While the storm creates a low-level thermodynamic environment more favorable for convection and an environment supportive of trapping its own gravity waves, convective cells do not initiate until the MABL moves in close proximity to the storm (Figs. 15 and 16; 195 min), implying that the MABL also plays a critical role. As the MABL moves across the domain, gravity waves are generated at its leading edge (Fig. 15). Given the absence of a critical layer, these waves propagate into the stratosphere; however, we hypothesize their role is twofold along their trajectory. First, the waves provide a mechanism for ascent within the layer of storm-enhanced instability between 1 and 4 km before they propagate into the stratosphere, which

the storm-generated gravity waves trapped within the mid- and upper troposphere are unable to provide. Alone, however, the MABL-generated waves are unable to initiate cells within the ambient conditionally unstable layer. The waves are incapable of generating cells until they arrive in the region of storm-enhanced instability. Their second role may be in the constructive interference with the storm-generated gravity waves. The combined impact of the lower-tropospheric MABL-generated waves and the mid- to upper-tropospheric storm-generated waves may lead to a layer of ascent with a sufficient depth and magnitude to support cell initiation in the presence of storm-enhanced low-level instability.

Similar conditions exist to support precollision cell development and wave trapping prior to the collision with the $-3\text{-K-}\theta'$ 1.5-km-deep MABL (Figs. 18–20). Ambient air lifted by the MABL oscillates vertically in association with the MABL-induced gravity waves, and fails rise above 2 km until in close proximity to the storm (Fig. 18). Conditional instability is present in the environment below 5 km, but again, is enhanced and confined to a 1–4-km layer immediately downstream of the storm, associated with a band of storm-reduced θ_{es} near 4 km and the MABL below 1 km (Fig. 19). Upper-troposphere static stability is reduced near the storm, visible in both the spatial and temporal evolution of N^2 (Fig. 20). As the storm approaches the region of cell development (270–290 km), stability decreases between 7 and 11 km and increases between 4 and 7 km, likely

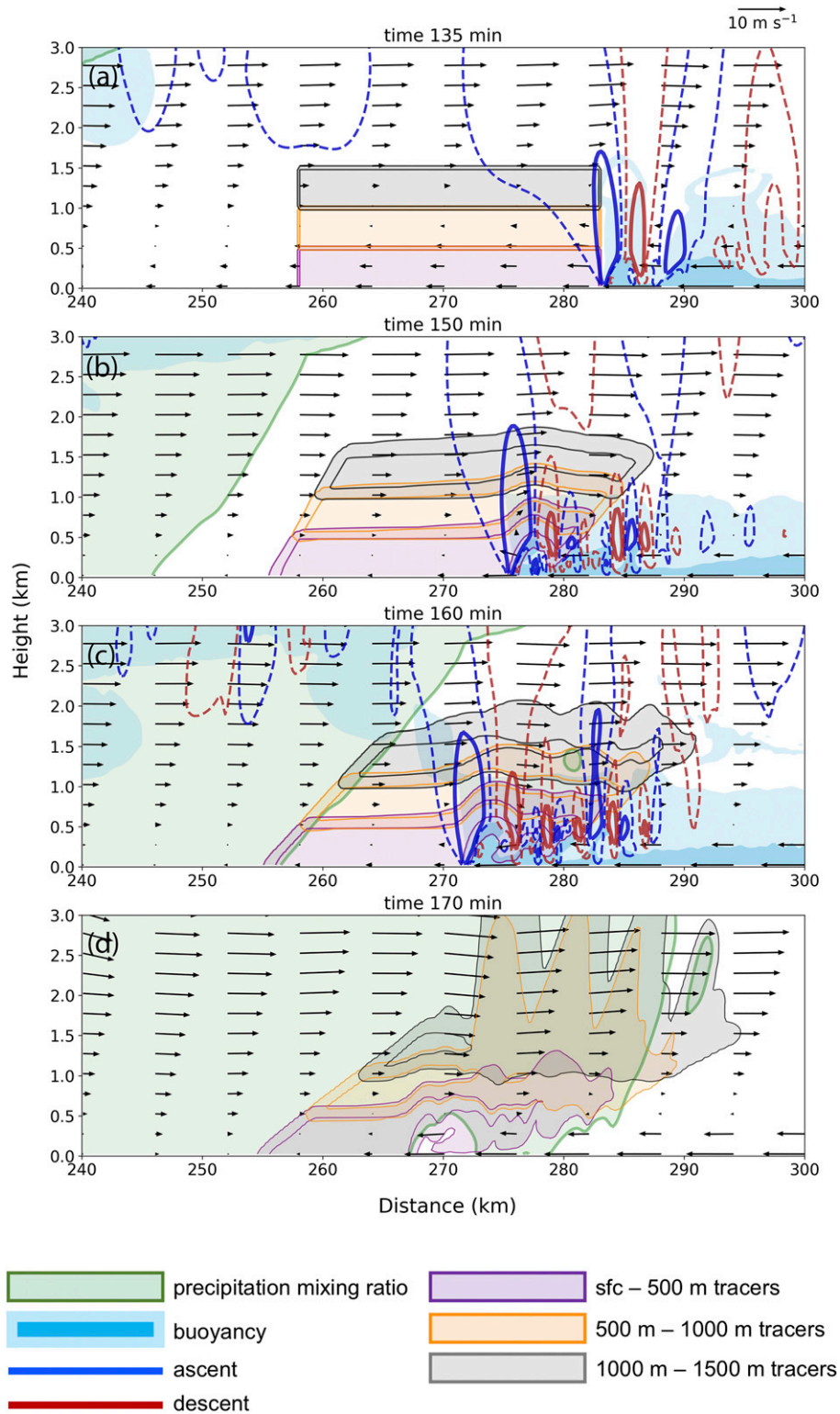


FIG. 18. As in Fig. 15, but with a $-3-K-\theta'$ 1.5-km-deep MABL at (a) 135, (b) 150, (c) 160, and (d) 170 min. Buoyancy and vertical motion are not included at 170 min.

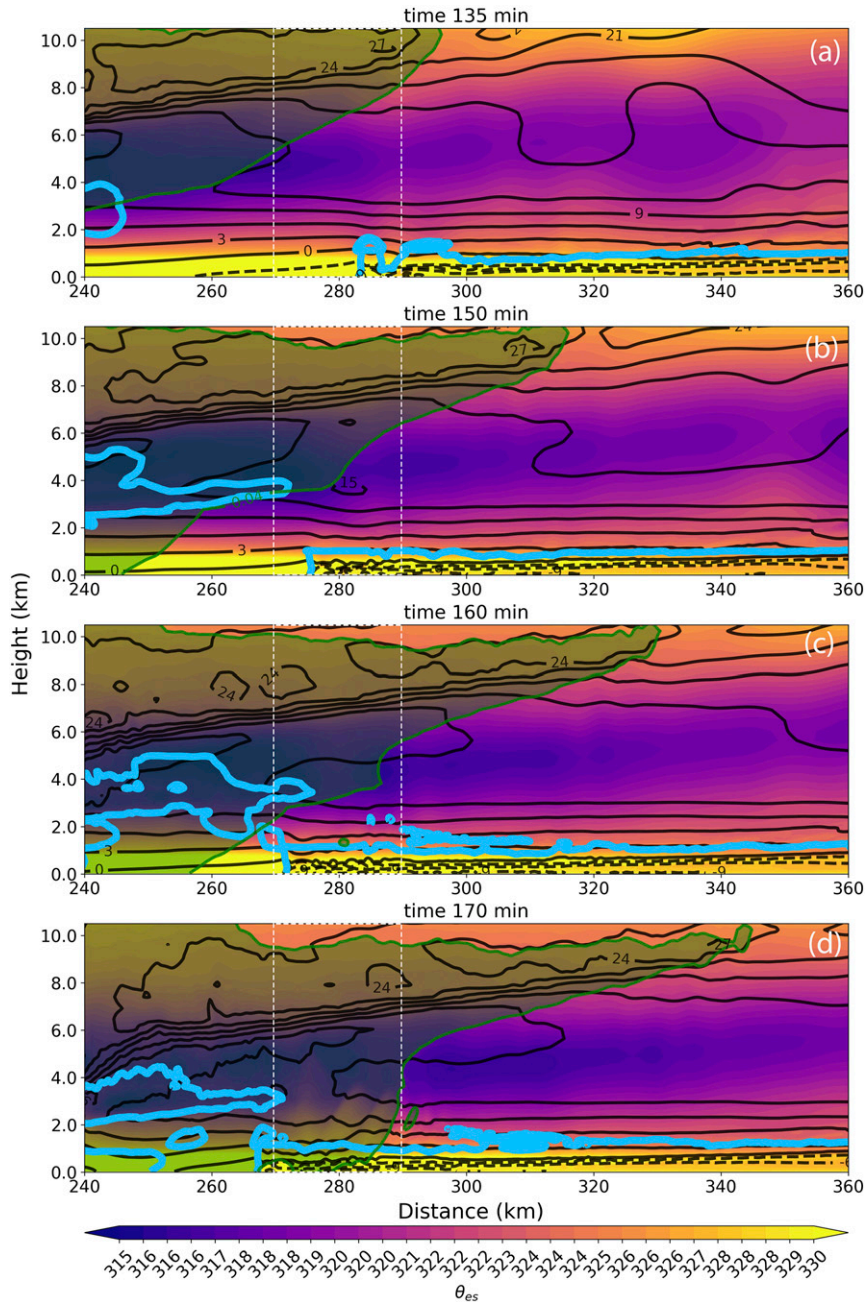


FIG. 19. As in Fig. 16, but with a $-3\text{-K-}\theta'$ 1.5-km-deep MABL at (a) 135, (b) 150, (c) 160, and (d) 170 min.

associated with diabatic processes (Figs. 19c,d and 20c,d).⁵ Again, instability is enhanced closer to the storm (260 km), with a trend toward a more statically stable troposphere farther away (400 km). Given the jet within the storm anvil approaches 27 m s^{-1} and the wave speed is estimated at 28 m s^{-1} (not

⁵ RH with respect to ice is maximized between 11 and 12 km and increases from 80% to near 100% between 135 and 170 min.

shown), $c - U$ likely approaches, but remains above, zero ($2\text{--}3\text{ m s}^{-1}$) based on this estimate of c .

While the discrete propagation of the squall lines presented here is due to a combination of storm- and MABL-generated gravity waves in the presence of storm-enhanced instability, different physical mechanisms can lead to this type of downstream cell development (Fovell et al. 2006). A reduction in the LFC in the storm-modified environment has been shown to support the initiation of isolated cells, the beginning stages of a

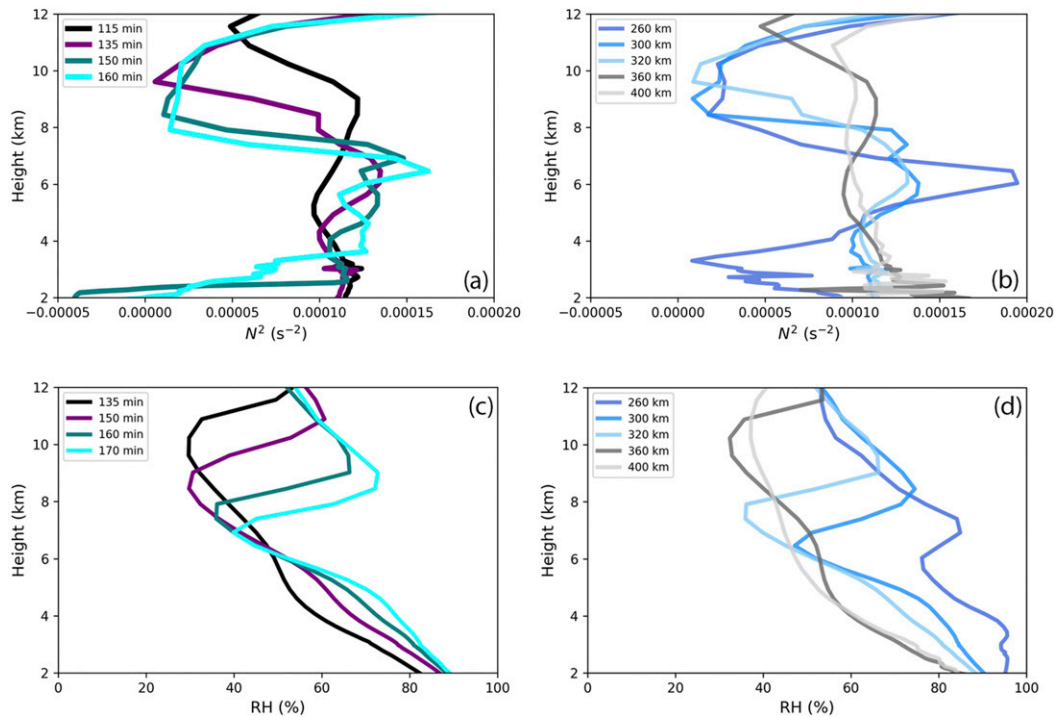


FIG. 20. As in Fig. 17, but with a $-3\text{-K-}\theta'$ 1.5-km-deep MABL (a) located at 280 km at 115 (black), 135 (purple), 150 (teal), and 160 min (cyan), and (b) at 170 min located at 260 (dark blue), 300 (blue), 320 (light blue), 360 (dark gray), and 400 km (light gray). (c) As is (a), but for relative humidity (RH, %) with respect to water. (d) As in (b), but for relative humidity (RH, %) with respect to water.

discrete propagation, by a “sufficiently deep” MABL once it moved into this environment (LK18). We hypothesized that a similar mechanism was responsible for the discrete propagation in the present study, though there were minimal changes to the LFC in the storm modified environment, indicating that other processes controlled the precollision cell formation.

e. Sensitivity to collision timing

The timing of the collision between the storm cold pool and the MABL is altered to ensure that the precollision cell development and precipitation peak are not dependent on a specific stage in the control storm’s life cycle. Further, within the mid-Atlantic, the distance between the Appalachian Mountains and the coastline increases moving from north to south. Given that the Appalachians are a common region for convective initiation (CI), storms will encounter the coast at different phases in their life cycle (*ceteris paribus*). These experiments provide some insight into the impact of the geographical distance between the location of CI and the coast, albeit limited insight given the large atmospheric and topographic parameter space. The collision time is delayed to 330 min (1.75 h later; Fig. 2). Only the two deep MABL experiments are presented. Again, isolated cells form downstream of both squall lines, indicating that cell initiation is not sensitive to storm age. Characteristics of cell development differ slightly from the earlier collision times, however, encompassing wider longitudinal bands and with CI occurring “sooner,” when the storms and MABLs are farther apart

(Fig. 21). Consequently, the associated increase in rain occurs sooner than for the earlier interaction times (Fig. 22). Storm lifetime is also extended, with more intense storms at later times (not shown) and longer periods of enhanced rain following the cold pool–MABL collisions (Fig. 22).

4. Discussion

a. Forcing mechanism versus precipitation

The bore and bore-hybrid features provided mechanisms to successfully move storms over the stable MABLs. While these features determine whether storms will survive and precipitate over the coastal waters, they do not govern the intensity of the precipitation. Considering storms moving over the deep MABLs, one may conclude that bore-forced storms will produce more precipitation, while hybrid-forced storms produce less (Fig. 3), though this is not always true. Storms moving over the shallower MABLs have similar precipitation, though are forced by different mechanisms. This was illustrated in section 3a, in which evidence indicated that the collective metrics for one storm were not clearly larger than the other, resulting in similar total rain. This speaks to the importance of the ambient conditions in determining storm intensity, specifically the control on the magnitude of the ascent of each lifting mechanism.

Section 3c presented evidence of the stability and vertical wind profile that support the development of the bore, cold pool–bore hybrid, and cold pool. Though SBCAPE

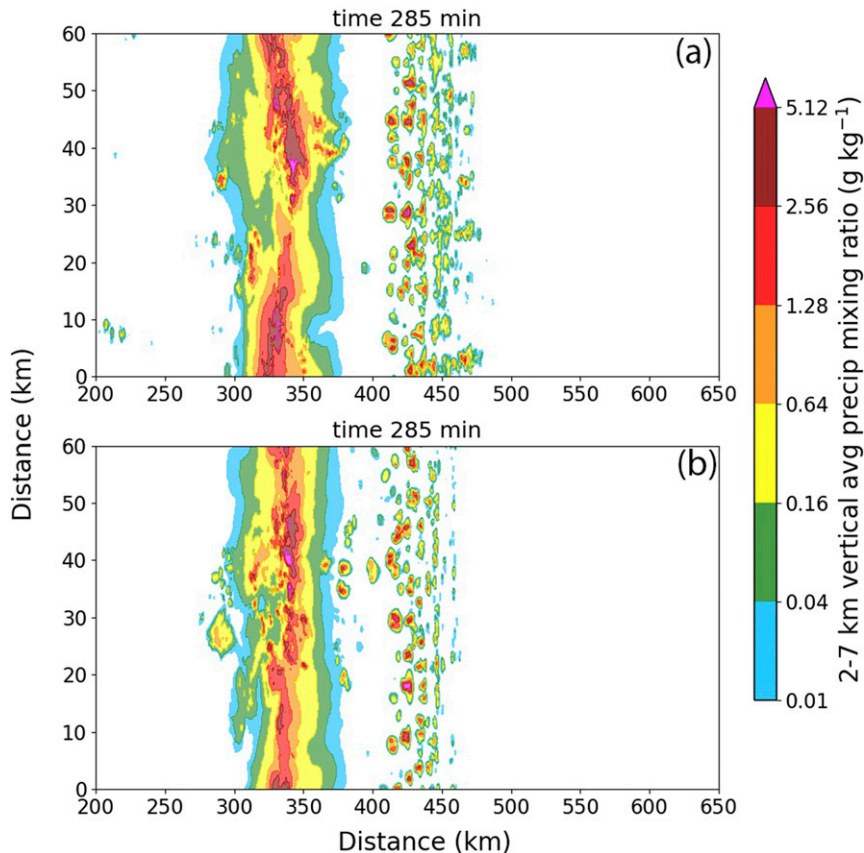


FIG. 21. Plan view of 2–7-km vertically averaged precipitation mixing ratio (g kg^{-1}) at 285 min for storms colliding with the 1.5-km-deep (a) $-6-$ and (b) $-3-\text{K}-\theta'$ MABL at approximately 330 min into the simulation.

(147 J kg^{-1}) and MUCAPE (687 J kg^{-1}) are low in the environment that supports bore development, the vertical profile in θ , θ_{es} , and the enhanced vertical wind shear profile ($>15 \text{ m s}^{-1}$ in the lowest 2.5 km), more importantly the flow opposing the bore motion at the lowest levels due to the moving MABL, support a robust bore with strong low-level vertical motion (Fig. 8) and vertical acceleration (Fig. 9) leading to intense convection. Winds within the lowest 1 km oppose the motion of the bore, with easterly wind values $>6 \text{ m s}^{-1}$, which has been shown to be critical in trapping wave energy at low-levels in both observations and numerical modeling (Doviak and Ge 1984; Crook 1988; Fulton et al. 1990). The vertical motion and acceleration of the hybrid feature are comparatively weaker, due to the less favorable environment for trapping gravity wave energy (as presented in section 3c), including a shallower layer of opposing winds (0.75 km deep) and a smaller peak easterly value within this layer of $<4 \text{ m s}^{-1}$. Regardless of the larger SBCAPE (583 J kg^{-1}) and similar MUCAPE (587 J kg^{-1}), convection is less intense due to the weaker forcing. This is true for the control storm as well, with comparatively large SBCAPE (1226 J kg^{-1}) and MUCAPE (1239 J kg^{-1}) but weak vertical motion, leading to the weakest convection. Therefore, the environmental factors controlling the magnitude of

the vertical motion of these features is the limiting factor, rather than the magnitude of the stability controlling the buoyant ascent.

Supportive evidence is provided by 2D simulated coastal squall lines in an RKW-type environment (LK18). Bores also formed following the collision between lower-buoyancy MABLs and higher-buoyancy cold pools, and hybrid features formed when the buoyancies were similar; however, storms forced by bores produced the least precipitation, storms forced by hybrid features produced more precipitation, and those forced by surface-based cold pools while over the MABL ($B_{\text{MABL}} > B_{\text{coldpool}}$) produced the most rain. These differences occurred in response to the magnitude of the ascent and vertical acceleration, rather than differences in CAPE. Vertical motion associated with the bore was the weakest, while that associated with the cold pool was the strongest due to the ambient conditions. Therefore, the buoyancy relationship between the cold pool and MABL can determine the physical ascent mechanism to support storms moving over the coastal waters, but the ambient stability and wind profile plays an important role in the associated precipitation development by determining the intensity of the vertical motion associated with each feature. The environment supports either the amplification or suppression of these lifting

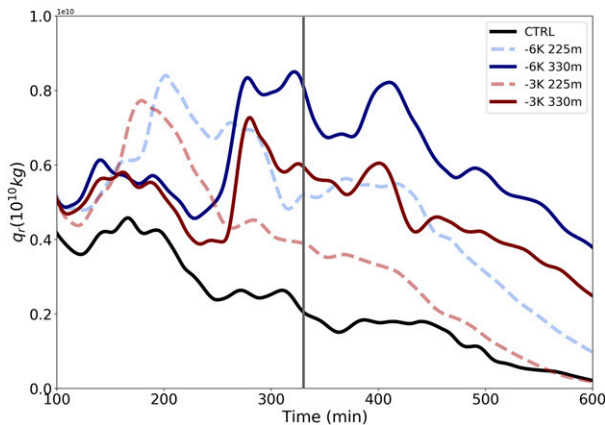


FIG. 22. Time series of the total mass of rain in the domain for control experiment with no MABL (black), storms interacting with the 1.5-km-deep $-6\text{-K-}\theta'$ (dashed light blue) and $-3\text{-K-}\theta'$ (dashed light red) MABL at 225 min, and storms interacting with the 1.5-km-deep $-6\text{-K-}\theta'$ (solid dark blue) and $-3\text{-K-}\theta'$ (solid dark red) MABL at 330 min. The gray line marks the approximate time of the delayed collision (330 min) between the storms and MABLs.

mechanisms, magnitude of the vertical motion, and thus the associated precipitation.

b. Implications for associated hazards

It has been shown that low-level coastal heterogeneities, specifically moving marine layers (i.e., sea breezes), modify squall line precipitation and dynamics. As such, this has implications for the resulting hazards and hazard prediction, which are addressed below.

- 1) Squall lines do not always weaken at the coast due to the MABL, but can actually intensify.
- 2) The development of precollision cells can increase the likelihood of flooding and flash flooding as storms approach the coast. Cell development is also associated with the discrete propagation of a storm; Cells become the storm's new leading edge during reorganization near the MABL boundary, causing the parent storm to weaken. Consequently, the leading edge of the storm appears to move faster than its translation speed, an apparent acceleration, and the associated hazards arrive sooner than anticipated. Effectively, this widens the region of convective precipitation as the storm undergoes reorganization. This is especially problematic in regions of offshore recreational, commercial, and military activities.
- 3) The peak in total rain associated with these precollision cells is sensitive to MABL depth, temperature, and maturity of the storm, which may be exploited for predictability.

5. Summary and conclusions

Cloud-resolving numerical simulations were used to isolate and quantify the impact of coastal moving marine boundary layers on squall lines, with a focus on storms over the U.S. mid-Atlantic. Storm sensitivity to a parameter space of MABL

characteristics, including depth and temperature, was explored. There are several important findings from this work. A squall line encountering and moving over a cold, deep (i.e., $-6\text{-K-}\theta'$ 1500-m) MABL can in fact intensify, with more convective updrafts and larger precipitation than in the absence of a MABL. Storm intensity was smaller in the presence of an equally deep, but relatively warmer ($-3\text{-K-}\theta'$) MABL. This indicates that squall line intensity can be sensitive to MABL temperature, but only for sufficiently deep MABLs. There were little differences in precipitation and updraft volume and intensity for storms moving over a -6- and a $-3\text{-K-}\theta'$ 750-m-deep MABL.

Mechanisms that propagate storms over the offshore stable layer is dependent on the buoyancy of the cold pool and MABL. The physical encounter between the two is relatively abrupt, leading the development of gravity wave-type features, which lift air parcels from above and within the upper portion of the MABL into the storm. A bore results from the collision when the buoyancy of the MABL is lower than that of the storm cold pool, while a hybrid cold pool-bore forms when the buoyancy of the two are similar, consistent with previous work. While these features provide a mechanism to move storms offshore, they do not necessarily determine storm intensity.

As squall lines and MABLs approach one another, the storms propagated discretely. A field of isolated convective cells formed downstream and parallel to the primary storm, and after reorganization, became the new leading line. This led to an apparent acceleration of the storm and an increase in precipitation prior to the storm cold pool-MABL collision. Cells formed through the interaction between storm- and MABL-generated gravity waves in the presence of storm-enhanced instability. As the MABLs moved across the domain, no convection resulted from the associated lift at their leading edges nor the gravity waves that emanated from the front; however, once the MABLs approached the storms, convection initiated indicating that cell development was due to a different mechanism. The squall lines modified their downstream environment, specifically by reducing upper-level stability (8–11 km) while stabilizing the midlevels (4–7 km), as well as increasing the upper-level winds through storm outflow. They also emanated high-frequency gravity waves. The energy of the waves was trapped in the favorable storm-modified environment, but propagated into the stratosphere further downstream. Alone, these waves were unable to generate the cells as well. Once the MABL and storm came in close contact, the constructive interference between the storm- and MABL-generated waves in the presence of a storm-modified stability vertical profile supported cell development. Cell development was insensitive to storm age, with cells developing downstream of more mature squall lines that encountered a MABL later in their life cycle.

For observed squall line events, the parameter space of MABL and environmental characteristics is large and dynamic, owing to the global extent over which coastal squall lines occur (midlatitudes to tropics). Simulating storms in this myriad of conditions is realistically unfeasible. Consistencies in the physical processes presented herein and our prior 2D work

using a different base state suggest that a comprehensive understanding of the dominant controls on coastal squall lines is attainable without such a laborious task. Further, implicit in this work is the sensitivity of coastal squall lines to small differences in MABL characteristics. MABL temperature and depth values were intentionally chosen to highlight the different possible regimes within the bounds of observations; a 1°–2°C difference in θ' and a 0.1–0.3-km difference in depth produced minimal differences in fundamental physical processes. Future work is needed to more rigorously test this sensitivity, as well as to include additional coastal complexities, such as orography.

Acknowledgments. This research would not have been possible without the generous support from the National Science Foundation Grant AGS-1514115, Office of Naval Research Grant N00014-16-1-3199, and Office of Naval Research Grant N00014-17-1-2478. The author would like to acknowledge high-performance computing support from Cheyenne (doi: 10.5065/D6RX99HX) provided by NCAR’s Computational and Information Systems Laboratory, sponsored by the National Science Foundation. The author would like to greatly thank Dr. George Bryan for the development and continued improvements of the CM1, and for the related insightful conversations. The author would also like to thank Dr. Matthew R. Kumjian for MATLAB assistance; Dr. Ryan Hastings for assistance in developing the “mid-Atlantic” thermodynamic profile and preliminary discussions regarding the numerical simulations; and the Editor Dr. Lou Wicker and three anonymous reviewers for their insightful comments.

APPENDIX

Analytic Thermodynamic Profile for the Mid-Atlantic Coastal Plain

For the “mid-Atlantic” thermodynamic profile, the vertical profile of potential temperature (θ) through the boundary layer is

$$\theta[k] = \left[(\theta_{bl} - \theta_{sfc}) \times \frac{z[k]}{D_{bl}} \right] + \theta_{sfc}, \tag{A1}$$

where $\theta_{bl} = 302$ K is the potential temperature at the top of the boundary layer, $\theta_{sfc} = 300$ K is the potential temperature at the surface, z is height (m) at the vertical grid point $[k]$, and $D_{bl} = 1000$ m is the depth of the boundary layer. From the top of the boundary layer to 12 km,

$$\theta[k] = \left[(343 - \theta_{bl}) \times \frac{z[k] - D_{bl}}{120\,000 - D_{bl}} \right] + \theta_{bl}, \tag{A2}$$

while above 12 km

$$\theta[k] = \left[87 \times \frac{z[k] - 120\,000}{8000} \right] + 343. \tag{A3}$$

The full vertical profile of the water vapor mixing ratio (q_v) is first determined by

$$q_v[k] = \frac{\varepsilon \times e[k]}{p[k] - e[k]}, \tag{A4}$$

ε is the ratio of the gas constant for dry air ($R_d = 287.04$ J kg⁻¹ K⁻¹) and the gas constant for water vapor ($R_v = 461$ J kg⁻¹ K⁻¹), e is the vapor pressure (Pa),

$$e = e_s \times RH, \tag{A5}$$

with the saturation vapor pressure (e_s),

$$e_s[k] = 611.2 \times \exp \left[\frac{17.67 \times T[k]}{T[k] + 243.5} \right], \tag{A6}$$

p is pressure (Pa) with the surface pressure specified as $p_{sfc} = 968$ hPa, T is temperature (°C), and RH is the relative humidity (%) held constant at 85%. The vertical profile of the vapor mixing ratio within the boundary layer ($q_{v(bl)}$) is then modified to

$$q_{v(bl)}[k] = \left[(q_{v(sfc)} - q_v[k]) \times \frac{z[k] - D_{bl}}{z[0] - D_{bl}} \right] + q_v[k], \tag{A7}$$

where $q_{v(sfc)}$ is the water vapor mixing ratio at the surface specified as 0.014 kg kg⁻¹. For reference, CAPE is approximately 400 J kg⁻¹ lower than for WK82, with a more saturated environment from the level of free convection (LFC) to 600 hPa.

REFERENCES

Alexander, M. J., and J. R. Holton, 2004: On the spectrum of vertically propagating gravity waves generated by a transient heat source. *Atmos. Chem. Phys.*, **4**, 923–932, <https://doi.org/10.5194/acp-4-923-2004>.

Blamey, R. C., and C. J. C. Reason, 2009: Numerical simulation of a mesoscale convective system over the east coast of South Africa. *Tellus*, **61**, 17–34, <https://doi.org/10.1111/j.1600-0870.2008.00366.x>.

Bosart, L. F., and A. Seimon, 1988: A case study of an unusually intense atmospheric gravity wave. *Mon. Wea. Rev.*, **116**, 1857–1886, [https://doi.org/10.1175/1520-0493\(1988\)116<1857:ACSOAU>2.0.CO;2](https://doi.org/10.1175/1520-0493(1988)116<1857:ACSOAU>2.0.CO;2).

Breeding, R. J., 1971: A non-linear investigation of critical levels for internal atmospheric gravity waves. *J. Fluid Mech.*, **50**, 545–563, <https://doi.org/10.1017/S0022112071002751>.

Bryan, G. H., and J. M. Fritsch, 2002: A benchmark for moist nonhydrostatic numerical models. *Mon. Wea. Rev.*, **130**, 2917–2928, [https://doi.org/10.1175/1520-0493\(2002\)130<2917:ABSFMN>2.0.CO;2](https://doi.org/10.1175/1520-0493(2002)130<2917:ABSFMN>2.0.CO;2).

Buzzi, A., M. Fantini, and G. Lippolis, 1991: Quasi-stationary organized convection in the presence of an inversion near the surface: Experiments with a 2-D numerical model. *Meteor. Atmos. Phys.*, **45**, 75–86, <https://doi.org/10.1007/BF01027476>.

Carbone, R. E., J. W. Conway, N. A. Crook, and M. W. Moncrieff, 1990: The generation and propagation of a nocturnal squall line. Part I: Observations and implications for mesoscale predictability. *Mon. Wea. Rev.*, **118**, 26–49, [https://doi.org/10.1175/1520-0493\(1990\)118<0026:TGAPOA>2.0.CO;2](https://doi.org/10.1175/1520-0493(1990)118<0026:TGAPOA>2.0.CO;2).

Clark, D. B., C. M. Taylor, A. J. Thorpe, R. J. Harding, and M. E. Nicholls, 2003: The influence of spatial variability of boundary-layer moisture on tropical continental squall lines. *Quart. J. Roy. Meteor. Soc.*, **129**, 1101–1121, <https://doi.org/10.1256/qj.02.122>.

- , —, and —, 2004: Feedback between the land surface and rainfall at convective length scales. *J. Hydrometeor.*, **5**, 625–639, [https://doi.org/10.1175/1525-7541\(2004\)005<0625:FBTLSA>2.0.CO;2](https://doi.org/10.1175/1525-7541(2004)005<0625:FBTLSA>2.0.CO;2).
- Clark, R. H., 1983: Fair weather nocturnal inland wind surges and atmospheric bores: Part I: Nocturnal wind surges. *Aust. Meteor. Mag.*, **31**, 133–145.
- , 1984: Colliding sea-breezes and the creation of internal atmospheric bore waves: Two-dimensional numerical studies. *Aust. Meteor. Mag.*, **32**, 207–226.
- Cohuet, J. B., R. Romero, V. Homar, V. Ducrocq, and C. Ramis, 2011: Initiation of a severe thunderstorm over the Mediterranean Sea. *Atmos. Res.*, **100**, 603–620, <https://doi.org/10.1016/j.atmosres.2010.11.002>.
- Crook, N. A., 1986: The effect of ambient stratification and moisture on the motion of atmospheric undular bores. *J. Atmos. Sci.*, **43**, 171–181, [https://doi.org/10.1175/1520-0469\(1986\)043<0171:TEOASA>2.0.CO;2](https://doi.org/10.1175/1520-0469(1986)043<0171:TEOASA>2.0.CO;2).
- , 1988: Trapping of low-level internal gravity waves. *J. Atmos. Sci.*, **45**, 1533–1541, [https://doi.org/10.1175/1520-0469\(1988\)045<1533:TOLLIG>2.0.CO;2](https://doi.org/10.1175/1520-0469(1988)045<1533:TOLLIG>2.0.CO;2).
- , and M. W. Moncrieff, 1988: The effect of large-scale convergence on the generation and maintenance of deep moist convection. *J. Atmos. Sci.*, **45**, 3606–3624, [https://doi.org/10.1175/1520-0469\(1988\)045<3606:TEOLSC>2.0.CO;2](https://doi.org/10.1175/1520-0469(1988)045<3606:TEOLSC>2.0.CO;2).
- Crosman, E. T., and J. D. Horel, 2010: Sea and lake breezes: A review of numerical studies. *Bound.-Layer Meteor.*, **137**, 1–29, <https://doi.org/10.1007/s10546-010-9517-9>.
- Davies-Jones, R. P., 2003: An expression for effective buoyancy in surroundings with horizontal density gradients. *J. Atmos. Sci.*, **60**, 2922–2925, [https://doi.org/10.1175/1520-0469\(2003\)060<2922:AEFEBI>2.0.CO;2](https://doi.org/10.1175/1520-0469(2003)060<2922:AEFEBI>2.0.CO;2).
- Deardorff, J. W., 1980: Stratocumulus-capped mixed layers derived from a three-dimensional model. *Bound.-Layer Meteor.*, **18**, 495–527, <https://doi.org/10.1007/BF00119502>.
- DeLonge, M. S., J. D. Fuentes, S. Chan, P. A. Kucera, E. Joseph, A. T. Gaye, and B. Daouada, 2010: Attributes of mesoscale convective systems at the land-ocean transition in Senegal during NASA African monsoon multidisciplinary analyses 2006. *J. Geophys. Res.*, **115**, D10213, <https://doi.org/10.1029/2009JD012518>.
- Doswell, C. A., and P. M. Markowski, 2004: Is buoyancy a relative quantity? *Mon. Wea. Rev.*, **132**, 853–863, [https://doi.org/10.1175/1520-0493\(2004\)132<0853:IBARQ>2.0.CO;2](https://doi.org/10.1175/1520-0493(2004)132<0853:IBARQ>2.0.CO;2).
- Doviak, R. J., and R. Ge, 1984: An atmospheric solitary gust observed with a Doppler radar, a tall tower and a surface network. *J. Atmos. Sci.*, **41**, 2559–2573, [https://doi.org/10.1175/1520-0469\(1984\)041<2559:AASGOW>2.0.CO;2](https://doi.org/10.1175/1520-0469(1984)041<2559:AASGOW>2.0.CO;2).
- Drosowsky, W., G. J. Holland, and R. K. Smith, 1989: Structure and evolution of north Australian cloud lines observed during AMEX Phase I. *Mon. Wea. Rev.*, **117**, 1181–1192, [https://doi.org/10.1175/1520-0493\(1989\)117<1181:SAEONA>2.0.CO;2](https://doi.org/10.1175/1520-0493(1989)117<1181:SAEONA>2.0.CO;2).
- Dudhia, J., M. W. Moncrieff, and D. W. K. So, 1987: The two-dimensional dynamics of west African squall lines. *Quart. J. Roy. Meteor. Soc.*, **113**, 121–146, <https://doi.org/10.1002/qj.49711347508>.
- Emanuel, K. A., 1994: *Atmospheric Convection*. Oxford University Press, 580 pp.
- Fovell, R. G., 2002: Upstream influence of numerically simulated squall line storms. *Quart. J. Roy. Meteor. Soc.*, **128**, 893–912, <https://doi.org/10.1256/0035900021643737>.
- , D. Durran, and J. R. Holton, 1992: Numerical simulations of convectively generated stratospheric gravity waves. *J. Atmos. Sci.*, **49**, 1427–1442, [https://doi.org/10.1175/1520-0469\(1992\)049<1427:NSOCGS>2.0.CO;2](https://doi.org/10.1175/1520-0469(1992)049<1427:NSOCGS>2.0.CO;2).
- , G. L. Mullendore, and S.-H. Kim, 2006: Discrete propagation of numerically simulated nocturnal squall lines. *Mon. Wea. Rev.*, **134**, 3735–3752, <https://doi.org/10.1175/MWR3268.1>.
- French, A. J., and M. D. Parker, 2010: The response of simulated nocturnal convective systems to a developing low-level jet. *J. Atmos. Sci.*, **67**, 3384–3408, <https://doi.org/10.1175/2010JAS3329.1>.
- Fulton, J., D. S. Zrnić, and R. J. Doviak, 1990: Initiation of a solitary wave family in the demise of a nocturnal thunderstorm density current. *J. Atmos. Sci.*, **47**, 319–337, [https://doi.org/10.1175/1520-0469\(1990\)047<0319:IOASWF>2.0.CO;2](https://doi.org/10.1175/1520-0469(1990)047<0319:IOASWF>2.0.CO;2).
- Futyan, J. M., and A. D. D. Genio, 2007: Deep convective system evolution over Africa and the tropical Atlantic. *J. Climate*, **20**, 5041–5060, <https://doi.org/10.1175/JCLI4297.1>.
- Garstang, M., H. L. Massie Jr., J. Halverson, S. Greco, and J. Scala, 1994: Amazon coastal squall lines. Part I: Structure and kinematics. *Mon. Wea. Rev.*, **122**, 608–622, [https://doi.org/10.1175/1520-0493\(1994\)122<0608:ACSLPI>2.0.CO;2](https://doi.org/10.1175/1520-0493(1994)122<0608:ACSLPI>2.0.CO;2).
- Geerts, B., and Coauthors, 2017: The 2015 plains elevated convection at night field project. *Bull. Amer. Meteor. Soc.*, **98**, 767–786, <https://doi.org/10.1175/BAMS-D-15-00257.1>.
- Greco, S., J. Scala, J. Halverson, H. L. Massie Jr., W.-K. Tao, and M. Garstang, 1994: Amazon coastal squall lines. Part II: Heat and moisture transports. *Mon. Wea. Rev.*, **122**, 623–635, [https://doi.org/10.1175/1520-0493\(1994\)122<0623:ACSLPI>2.0.CO;2](https://doi.org/10.1175/1520-0493(1994)122<0623:ACSLPI>2.0.CO;2).
- Haase, S. P., and R. K. Smith, 1984: Morning glory wave clouds in Oklahoma: A case study. *Mon. Wea. Rev.*, **112**, 2078–2089, [https://doi.org/10.1175/1520-0493\(1984\)112<2078:MGWCIO>2.0.CO;2](https://doi.org/10.1175/1520-0493(1984)112<2078:MGWCIO>2.0.CO;2).
- , and —, 1989: The numerical simulation of atmospheric gravity currents. Part II: Environments with stable layers. *Geophys. Astrophys. Fluid Dyn.*, **46**, 35–51, <https://doi.org/10.1080/03091928908208903>.
- Haghi, K. R., and Coauthors, 2019: Bore-ing into nocturnal convection. *Bull. Amer. Meteor. Soc.*, **100**, 1103–1121, <https://doi.org/10.1175/BAMS-D-17-0250.1>.
- Ichikawa, H., and T. Yasunari, 2007: Propagating diurnal disturbances embedded in the Madden-Julian oscillation. *Geophys. Res. Lett.*, **34**, L18811, <https://doi.org/10.1029/2007GL030480>.
- Jeevanjee, N., and D. M. Romps, 2015: Effective buoyancy, inertial pressure, and the mechanical generation of buoyancy-layer mass flux by cold pools. *J. Atmos. Sci.*, **72**, 3199–3213, <https://doi.org/10.1175/JAS-D-14-0349.1>.
- Keyser, D., and R. A. Anthes, 1977: The applicability of a mixed-layer model of the planetary boundary layer to real-data forecasting. *Mon. Wea. Rev.*, **105**, 1351–1371, [https://doi.org/10.1175/1520-0493\(1977\)105<1351:TAOAMM>2.0.CO;2](https://doi.org/10.1175/1520-0493(1977)105<1351:TAOAMM>2.0.CO;2).
- Kingsmill, D. E., and N. A. Crook, 2003: An observational study of atmospheric bore formation from colliding density currents. *Mon. Wea. Rev.*, **131**, 2985–3002, [https://doi.org/10.1175/1520-0493\(2003\)131<2985:AOSOAB>2.0.CO;2](https://doi.org/10.1175/1520-0493(2003)131<2985:AOSOAB>2.0.CO;2).
- Klemp, J. B., and R. B. Wilhelmson, 1978: The simulation of three-dimensional convective storm dynamics. *J. Atmos. Sci.*, **35**, 1070–1096, [https://doi.org/10.1175/1520-0469\(1978\)035<1070:TSOTDC>2.0.CO;2](https://doi.org/10.1175/1520-0469(1978)035<1070:TSOTDC>2.0.CO;2).
- Knupp, K. R., 2006: Observational analysis of a gust from to bore to solitary wave transition within an evolving nocturnal boundary layer. *J. Atmos. Sci.*, **63**, 2016–2035, <https://doi.org/10.1175/JAS3731.1>.

- Koch, S. E., P. B. Dorian, R. Ferrare, S. H. Melfi, W. C. Skillman, and D. Whiteman, 1991: Structure of an internal bore and dissipating gravity current as revealed by Raman lidar. *Mon. Wea. Rev.*, **119**, 857–887, [https://doi.org/10.1175/1520-0493\(1991\)119<0857:SOAIBA>2.0.CO;2](https://doi.org/10.1175/1520-0493(1991)119<0857:SOAIBA>2.0.CO;2).
- Kömüşçü, A. Ü., A. Erkan, and S. Çelik, 1998: Analysis of meteorological and terrain features leading to the İzmir flash flood, 3–4 November 1995. *Nat. Hazards*, **18**, 1–25, <https://doi.org/10.1023/A:1008078920113>.
- Kurz, M., and A. D. Fontana, 2004: A case of cyclogenesis over the western Mediterranean Sea with extraordinary convective activity. *Meteor. Appl.*, **11**, 97–113, <https://doi.org/10.1017/S1350482704001161>.
- LeMone, M. A., E. J. Zipser, and S. B. Trier, 1998: The role of environmental shear and thermodynamic conditions in determining the structure and evolution of mesoscale convective systems during TOGA COARE. *J. Atmos. Sci.*, **55**, 3493–3518, [https://doi.org/10.1175/1520-0469\(1998\)055<3493:TROESA>2.0.CO;2](https://doi.org/10.1175/1520-0469(1998)055<3493:TROESA>2.0.CO;2).
- Lensky, I. M., and S. Schiff, 2007: Using MSG to monitor the evolution of severe convective storms over east Mediterranean Sea and Israel, and its response to aerosol loading. *Ann. Glaciol.*, **112**, 95–100, <https://doi.org/10.5194/adgeo-12-95-2007>.
- Lericos, T. P., H. E. Fuelberg, M. L. Weisman, and A. I. Watson, 2007: Numerical simulations of the effects of coastlines on the evolution of strong, long-lived squall lines. *Mon. Wea. Rev.*, **135**, 1710–1731, <https://doi.org/10.1175/MWR3381.1>.
- Letkewicz, C. E., and M. D. Parker, 2010: Forecasting the maintenance of mesoscale convective systems crossing the Appalachian Mountains. *Wea. Forecasting*, **25**, 1179–1195, <https://doi.org/10.1175/2010WAF2222379.1>.
- Li, J., B. Wang, and D.-H. Wang, 2012: The characteristics of mesoscale convective systems (MCSs) over East Asia in warm seasons. *Atmos. Oceanic Sci. Lett.*, **5**, 102–107, <https://doi.org/10.1080/16742834.2012.11446973>.
- Lin, Y.-L., 2007: *Mesoscale Dynamics*. Cambridge University Press, 630 pp.
- , and R. G. Goff, 1988: A study of a mesoscale solitary wave in the atmosphere originating near a region of deep convection. *J. Atmos. Sci.*, **45**, 194–206, [https://doi.org/10.1175/1520-0469\(1988\)045<0194:ASOAMS>2.0.CO;2](https://doi.org/10.1175/1520-0469(1988)045<0194:ASOAMS>2.0.CO;2).
- Lindzen, R. S., and K.-K. Tung, 1976: Banded convective activity and ducted gravity waves. *Mon. Wea. Rev.*, **104**, 1602–1617, [https://doi.org/10.1175/1520-0493\(1976\)104<1602:BCAADG>2.0.CO;2](https://doi.org/10.1175/1520-0493(1976)104<1602:BCAADG>2.0.CO;2).
- Lombardo, K., and B. A. Colle, 2010: The spatial and temporal distribution of organized convective structures over the Northeast and their ambient conditions. *Mon. Wea. Rev.*, **138**, 4456–4474, <https://doi.org/10.1175/2010MWR3463.1>.
- , and —, 2011: Convective storm structures and ambient conditions associated with severe weather over the northeast United States. *Wea. Forecasting*, **26**, 940–956, <https://doi.org/10.1175/WAF-D-11-00002.1>.
- , and —, 2012: Ambient conditions associated with the maintenance and decay of quasi-linear convective systems crossing the northeastern U.S. coast. *Mon. Wea. Rev.*, **140**, 3805–3819, <https://doi.org/10.1175/MWR-D-12-00050.1>.
- , and —, 2013: Processes controlling the structure and longevity of two quasi-linear convective systems crossing the southern New England coast. *Mon. Wea. Rev.*, **141**, 3710–3734, <https://doi.org/10.1175/MWR-D-12-00336.1>.
- , and T. Kading, 2018: The behavior of squall lines in horizontally heterogeneous coastal environments. *J. Atmos. Sci.*, **75**, 1243–1269, <https://doi.org/10.1175/JAS-D-17-0248.1>.
- , E. Sinsky, Y. Jia, M. M. Whitney, and J. Edson, 2016: Sensitivity of simulated sea breezes to initial conditions in complex coastal regions. *Mon. Wea. Rev.*, **144**, 1299–1320, <https://doi.org/10.1175/MWR-D-15-0306.1>.
- , —, J. Edson, M. M. Whitney, and Y. Jia, 2018: Sensitivity of offshore surface fluxes and sea breezes to the spatial distribution of sea-surface temperature. *Bound.-Layer Meteor.*, **166**, 475–502, <https://doi.org/10.1007/s10546-017-0313-7>.
- Loveless, D. M., T. J. Wagner, D. D. Turner, S. A. Ackerman, and W. F. Feltz, 2019: A composite perspective on bore passages during the PECAN campaign. *Mon. Wea. Rev.*, **147**, 1395–1413, <https://doi.org/10.1175/MWR-D-18-0291.1>.
- Marshall, J. H., S. B. Trier, T. M. Weckwerth, and J. W. Wilson, 2011: Observations of elevated convection initiation leading to a surface-based squall line during 13 June IHOP_2002. *Mon. Wea. Rev.*, **139**, 247–271, <https://doi.org/10.1175/2010MWR3422.1>.
- Mattos, E. V., and L. A. T. Machado, 2011: Cloud-to-ground lightning and mesoscale convective systems. *Atmos. Res.*, **99**, 377–390, <https://doi.org/10.1016/j.atmosres.2010.11.007>.
- Meng, Z., D. Yan, and Y. Zhang, 2013: General features of squall lines in east China. *Mon. Wea. Rev.*, **141**, 1629–1647, <https://doi.org/10.1175/MWR-D-12-00208.1>.
- Miller, S. T. K., B. D. Keim, R. W. Talbot, and H. Mao, 2003: Sea breeze: Structure, forecasting, and impacts. *Rev. Geophys.*, **41**, 1011, <https://doi.org/10.1029/2003RG000124>.
- Morel, C., and S. Senesi, 2002a: A climatology of mesoscale convective systems over Europe using satellite infrared imagery. I: Methodology. *Quart. J. Roy. Meteor. Soc.*, **128**, 1953–1971, <https://doi.org/10.1256/003590002320603485>.
- , and —, 2002b: A climatology of mesoscale convective systems over Europe using satellite infrared imagery. II: Characteristics of European mesoscale convective systems. *Quart. J. Roy. Meteor. Soc.*, **128**, 1973–1995, <https://doi.org/10.1256/003590002320603494>.
- Morrison, H., G. Thompson, and V. Tatarski, 2009: Impact of cloud microphysics on the development of trailing stratiform precipitation in a simulated squall line: Comparison of one- and two-moment schemes. *Mon. Wea. Rev.*, **137**, 991–1007, <https://doi.org/10.1175/2008MWR2556.1>.
- , J. A. Milbrant, G. Bryan, S. A. Tessendorf, and G. Thompson, 2015: Parameterization of cloud microphysical based in the prediction of bulk ice particle properties. Part II: Case study comparisons with observations and other schemes. *J. Atmos. Sci.*, **72**, 312–339, <https://doi.org/10.1175/JAS-D-14-0066.1>.
- Nicholls, M. E., R. A. Pielke, and W. R. Cotton, 1991: Thermally forced gravity waves in an atmosphere at rest. *J. Atmos. Sci.*, **48**, 1869–1884, [https://doi.org/10.1175/1520-0469\(1991\)048<1869:TFGWIA>2.0.CO;2](https://doi.org/10.1175/1520-0469(1991)048<1869:TFGWIA>2.0.CO;2).
- Noonan, J. A., and R. K. Smith, 1986: Sea-breeze circulations over Cape York Pennsylvania and the generation of Gulf of Carpentaria cloud line disturbances. *J. Atmos. Sci.*, **43**, 1679–1693, [https://doi.org/10.1175/1520-0469\(1986\)043<1679:SBCOCY>2.0.CO;2](https://doi.org/10.1175/1520-0469(1986)043<1679:SBCOCY>2.0.CO;2).
- , and —, 1987: The generation of north Australia cloud lines and the ‘morning glory’. *Aust. Meteor. Mag.*, **35**, 31–45.
- Nunalee, C. G., and S. Basu, 2014: Mesoscale modeling of coastal low-level jets: Implications for offshore wind resource estimation. *Wind Energy*, **17**, 1199–1216, <https://doi.org/10.1002/we.1628>.
- Parker, M., 2008: Response of simulated squall lines to low-level cooling. *J. Atmos. Sci.*, **65**, 1323–1341, <https://doi.org/10.1175/2007JAS2507.1>.

- Parker, M. D., and R. H. Johnson, 2004: Simulated convective lines with leading precipitation. Part II: Evolution and maintenance. *J. Atmos. Sci.*, **61**, 1656–1673, [https://doi.org/10.1175/1520-0469\(2004\)061<1656:SCLWLP>2.0.CO;2](https://doi.org/10.1175/1520-0469(2004)061<1656:SCLWLP>2.0.CO;2).
- Parsons, D. B., K. R. Haghi, K. T. Halbert, and B. Elmer, 2019: The potential role of atmospheric bores and gravity waves in the initiation and maintenance of nocturnal convection over the southern Great Plains. *J. Atmos. Sci.*, **76**, 43–68, <https://doi.org/10.1175/JAS-D-17-0172.1>.
- Peters, K., and C. Hohenegger, 2017: The dependence of squall line characteristics on surface conditions. *J. Atmos. Sci.*, **74**, 2211–2228, <https://doi.org/10.1175/JAS-D-16-0290.1>.
- Rottman, J. W., and J. E. Simpson, 1989: The formation of internal bores in the atmosphere: A laboratory model. *Quart. J. Roy. Meteor. Soc.*, **115**, 941–963, <https://doi.org/10.1002/qj.49711548809>.
- Rotunno, R., J. B. Klemp, and M. L. Weisman, 1988: A theory for strong, long-lived squall lines. *J. Atmos. Sci.*, **45**, 463–485, [https://doi.org/10.1175/1520-0469\(1988\)045<0463:ATFSL>2.0.CO;2](https://doi.org/10.1175/1520-0469(1988)045<0463:ATFSL>2.0.CO;2).
- Ruppert, J. H., and L. F. Bosart, 2014: A case study of the interaction of a mesoscale gravity wave with a mesoscale convective system. *Mon. Wea. Rev.*, **142**, 1403–1429, <https://doi.org/10.1175/MWR-D-13-00274.1>.
- Salio, P., M. Nicolini, and E. Zipser, 2007: Mesoscale convective systems over southeastern South America and their relationship with the South American low-level jet. *Mon. Wea. Rev.*, **135**, 1290–1309, <https://doi.org/10.1175/MWR3305.1>.
- Schmidt, J. M., and W. R. Cotton, 1990: Interactions between upper and lower tropospheric gravity waves in squall line structure and maintenance. *J. Atmos. Sci.*, **47**, 1205–1222, [https://doi.org/10.1175/1520-0469\(1990\)047<1205:IBUALT>2.0.CO;2](https://doi.org/10.1175/1520-0469(1990)047<1205:IBUALT>2.0.CO;2).
- Schumacher, R. S., 2009: Mechanisms for quasi-stationary behavior in simulated heavy-rain-producing convective systems. *J. Atmos. Sci.*, **66**, 1543–1568, <https://doi.org/10.1175/2008JAS2856.1>.
- , 2015: Sensitivity of precipitation accumulation in elevated convective systems to small changes in low-level moisture. *J. Atmos. Sci.*, **72**, 2507–2524, <https://doi.org/10.1175/JAS-D-14-0389.1>.
- Shu, C.-W., 2001: High order finite difference and finite volume WENO schemes and discontinuous Galerkin methods for CFD. CASE Rep. 2001-11 NASA/CR-2001-210865, 16 pp.
- Simpson, J. E., 1982: Gravity currents in the laboratory, atmosphere, and ocean. *Annu. Rev. Fluid Mech.*, **14**, 213–234, <https://doi.org/10.1146/annurev.fl.14.010182.001241>.
- Smith, R. K., 1986: Evening glory wave-cloud lines in northwestern Australia. *Aust. Meteor. Mag.*, **34**, 27–33.
- Taylor, C. M., F. Saïd, and T. Lebel, 1997: Interactions between the land surface and mesoscale convective rainfall variability during HAPEX-Sahel. *Mon. Wea. Rev.*, **125**, 2211–2227, [https://doi.org/10.1175/1520-0493\(1997\)125<2211:IBTLA>2.0.CO;2](https://doi.org/10.1175/1520-0493(1997)125<2211:IBTLA>2.0.CO;2).
- Thorpe, A. J., M. J. Miller, and M. W. Moncrieff, 1982: Two-dimensional convection in non-constant shear: A model of mid-latitude squall lines. *Quart. J. Roy. Meteor. Soc.*, **108**, 739–762, <https://doi.org/10.1002/qj.49710845802>.
- Trier, S. B., C. A. Davis, A. Ahijevych, M. L. Weisman, and G. H. Bryan, 2006: Mechanisms supporting long-lived episodes of propagating nocturnal convection within a 7-day WRF Model simulation. *J. Atmos. Sci.*, **63**, 2437–2461, <https://doi.org/10.1175/JAS3768.1>.
- , J. H. Marsham, C. A. Davis, and D. A. Ahijevych, 2011: Numerical simulations of the postsunrise reorganization of a nocturnal mesoscale convective system during 13 June IHOP_2002. *J. Atmos. Sci.*, **68**, 2988–3011, <https://doi.org/10.1175/JAS-D-11-0112.1>.
- Tuduri, E., and C. Ramis, 1997: The environments of significant convective events in the western Mediterranean. *Wea. Forecasting*, **12**, 294–306, [https://doi.org/10.1175/1520-0434\(1997\)012<0294:TEOSCE>2.0.CO;2](https://doi.org/10.1175/1520-0434(1997)012<0294:TEOSCE>2.0.CO;2).
- van Delden, A., 1998: The synoptic setting of a thunder low and associated prefrontal squall line in western Europe. *Meteor. Atmos. Phys.*, **65**, 113–131, <https://doi.org/10.1007/BF01030272>.
- Wakimoto, R. M., and D. E. Kingsmill, 1995: Structure of an atmospheric undular bore generated from colliding boundaries during CaPE. *Mon. Wea. Rev.*, **123**, 1374–1393, [https://doi.org/10.1175/1520-0493\(1995\)123<1374:SOAAUB>2.0.CO;2](https://doi.org/10.1175/1520-0493(1995)123<1374:SOAAUB>2.0.CO;2).
- Wang, J.-J., and L. D. Carey, 2005: The development and structure of an oceanic squall line system during the South China Sea Monsoon Experiment. *Mon. Wea. Rev.*, **133**, 1544–1561, <https://doi.org/10.1175/MWR2933.1>.
- Wang, T.-A., and Y.-L. Lin, 1999: Wave ducting in a stratified shear flow over a two-dimensional mountain. Part I: General linear theory. *J. Atmos. Sci.*, **56**, 412–436, [https://doi.org/10.1175/1520-0469\(1999\)056<0412:WDIASS>2.0.CO;2](https://doi.org/10.1175/1520-0469(1999)056<0412:WDIASS>2.0.CO;2).
- Warner, T. T., B. E. Mapes, and M. Xu, 2003: Diurnal pattern of rainfall in northwestern south America. Part II: Model simulations. *Mon. Wea. Rev.*, **131**, 813–829, [https://doi.org/10.1175/1520-0493\(2003\)131<0813:DPORIN>2.0.CO;2](https://doi.org/10.1175/1520-0493(2003)131<0813:DPORIN>2.0.CO;2).
- Weisman, M. L., and J. B. Klemp, 1982: The dependence of numerically simulated convective storms on vertical wind shear and buoyancy. *Mon. Wea. Rev.*, **110**, 504–520, [https://doi.org/10.1175/1520-0493\(1982\)110<0504:TDonSC>2.0.CO;2](https://doi.org/10.1175/1520-0493(1982)110<0504:TDonSC>2.0.CO;2).
- , and —, 1984: The structure and classification of numerically simulated convective storms in directionally varying wind shears. *Mon. Wea. Rev.*, **112**, 2479–2498, [https://doi.org/10.1175/1520-0493\(1984\)112<2479:TSACON>2.0.CO;2](https://doi.org/10.1175/1520-0493(1984)112<2479:TSACON>2.0.CO;2).
- , and R. Rotunno, 2004: “A theory for strong long-lived squall lines” revisited. *J. Atmos. Sci.*, **61**, 361–382, [https://doi.org/10.1175/1520-0469\(2004\)061<0361:ATFSL>2.0.CO;2](https://doi.org/10.1175/1520-0469(2004)061<0361:ATFSL>2.0.CO;2).
- , J. B. Klemp, and R. Rotunno, 1988: Structure and evolution of numerically simulated squall lines. *J. Atmos. Sci.*, **45**, 1990–2013, [https://doi.org/10.1175/1520-0469\(1988\)045<1990:SAEONS>2.0.CO;2](https://doi.org/10.1175/1520-0469(1988)045<1990:SAEONS>2.0.CO;2).
- Wicker, L. J., and W. C. Skamarock, 2002: Time-splitting methods for elastic models using forward time schemes. *Mon. Wea. Rev.*, **130**, 2088–2097, [https://doi.org/10.1175/1520-0493\(2002\)130<2088:TSMFEM>2.0.CO;2](https://doi.org/10.1175/1520-0493(2002)130<2088:TSMFEM>2.0.CO;2).
- Wolters, D., C. C. van Heerwaarden, J. V.-G. de Arllano, B. Cappelaere, and D. Ramier, 2010: Effects of soil moisture gradients on the path and the intensity of a West African squall line. *Quart. J. Roy. Meteor. Soc.*, **136**, 2162–2175, <https://doi.org/10.1002/qj.712>.
- Yuan, J., and R. A. Houze, 2010: Global variability of mesoscale convective system anvil structure from A-Train satellite data. *J. Climate*, **23**, 5864–5888, <https://doi.org/10.1175/2010JCLI3671.1>.
- Zhang, J., D. B. Parsons, and Y. Wang, 2020: Wave disturbances and their role in the maintenance, structure, and evolution of a mesoscale convective system. *J. Atmos. Sci.*, **77**, 51–77, <https://doi.org/10.1175/JAS-D-18-0348.1>.